NeuroImage 215 (2020) 116800

Contents lists available at ScienceDirect

NeuroImage

journal homepage: www.elsevier.com/locate/neuroimage

Towards HCP-Style macaque connectomes: 24-Channel 3T multi-array coil, MRI sequences and preprocessing

Joonas A. Autio [a], Matthew F. Glasser [b,c,d], Takayuki Ose [a], Chad J. Donahue [b], Matteo Bastiani [e,f,m], Masahiro Ohno [a], Yoshihiko Kawabata [g], Yuta Urushibata [h], Katsutoshi Murata [h], Kantaro Nishigori [a,i], Masataka Yamaguchi [a,i], Yuki Hori [a], Atsushi Yoshida [a], Yasuhiro Go [j,k,l], Timothy S. Coalson [b], Saad Jbabdi [e], Stamatios N. Sotiropoulos [e,f,m], Henry Kennedy [n,o,p,q], Stephen Smith [e], David C. Van Essen [b], Takuya Hayashi [a,*]

[a] Laboratory for Brain Connectomics Imaging, RIKEN Center for Biosystems Dynamics Research, Kobe, Japan
[b] Department of Neuroscience, Washington University School of Medicine, St Louis, Missouri, USA
[c] Department of Radiology, Washington University School of Medicine, St Louis, MO, USA
[d] St. Luke's Hospital, St. Louis, Missouri, USA
[e] Wellcome Centre for Integrative Neuroimaging, Centre for Functional Magnetic Resonance Imaging of the Brain (FMRIB), University of Oxford, Oxford, United Kingdom
[f] Sir Peter Mansfield Imaging Centre, School of Medicine, University of Nottingham, Nottingham, United Kingdom
[g] Takashima Seisakusho Co., Ltd, Tokyo, Japan
[h] Siemens Healthcare Japan, Tokyo, Japan
[i] Sumitomo Dainippon Pharma Co., Ltd, Osaka, Japan
[j] Cognitive Genomics Research Group, Exploratory Research Center on Life and Living Systems, National Institutes of Natural Sciences, Okazaki, Japan
[k] Department of System Neuroscience, National Institute for Physiological Sciences, Okazaki, Japan
[l] Department of Physiological Sciences, School of Life Science, SOKENDAI (The Graduate University for Advanced Studies), Okazaki, Japan
[m] National Institute for Health Research (NIHR) Nottingham Biomedical Research Centre, Queens Medical Centre, Nottingham, UK
[n] Université Lyon, Université Claude Bernard Lyon, France
[o] Inserm, Stem Cell and Brain Research Institute, Bron, France
[p] Institute of Neuroscience, Key Laboratory of Primate Neurobiology, Center for Excellence in Brain Science and Intelligence Technology, Chinese Academy of Sciences, Shanghai, China
[q] Shanghai Center for Brain Science and Brain-Inspired Intelligence Technology, Shanghai, China

ARTICLE INFO

Keywords:
Macaque
Primate
Human connectome project
Parallel imaging
Cortex
Resting-state
Diffusion

ABSTRACT

Macaque monkeys are an important animal model where invasive investigations can lead to a better understanding of the cortical organization of primates including humans. However, the tools and methods for noninvasive image acquisition (e.g. MRI RF coils and pulse sequence protocols) and image data preprocessing have lagged behind those developed for humans. To resolve the structural and functional characteristics of the smaller macaque brain, high spatial, temporal, and angular resolutions combined with high signal-to-noise ratio are required to ensure good image quality. To address these challenges, we developed a macaque 24-channel receive coil for 3-T MRI with parallel imaging capabilities. This coil enables adaptation of the Human Connectome Project (HCP) image acquisition protocols to the in-vivo macaque brain. In addition, we adapted HCP preprocessing methods to the macaque brain, including spatial minimal preprocessing of structural, functional MRI (fMRI), and diffusion MRI (dMRI). The coil provides the necessary high signal-to-noise ratio and high efficiency in data acquisition, allowing four- and five-fold accelerations for dMRI and fMRI. Automated FreeSurfer segmentation of cortex, reconstruction of cortical surface, removal of artefacts and nuisance signals in fMRI, and distortion correction of dMRI all performed well, and the overall quality of basic neurobiological measures was comparable with those for the HCP. Analyses of functional connectivity in fMRI revealed high sensitivity as compared with those from publicly shared datasets. Tractography-based connectivity estimates correlated with tracer connectivity similarly to that achieved using ex-vivo dMRI. The resulting HCP-style in vivo macaque MRI data show

* Corresponding author. Laboratory for Brain Connectomics Imaging, RIKEN Center for Biosystems Dynamics Research, 6-7-3 Minatojima-minamimachi, Chuo-ku, Kobe, 650-0047, Japan.
E-mail address: takuya.hayashi@riken.jp (T. Hayashi).

https://doi.org/10.1016/j.neuroimage.2020.116800
Received 25 December 2019; Received in revised form 16 March 2020; Accepted 23 March 2020
Available online 8 April 2020

considerable promise for analyzing cortical architecture and functional and structural connectivity using advanced methods that have previously only been available in studies of the human brain.

1. Introduction

Old World monkeys are an important neuroscientific model for understanding primate neuroanatomy (Brodmann K., 1905; Felleman and Van Essen, 1991; Van Essen et al., 2001). Macaque monkeys have provided insights about neurovascular coupling (Goense and Logothetis, 2008), neural wiring (Markov et al., 2014) and the evolution of the human brain's functional connectome (Passingham, 2009; Wang et al., 2012). However, macaques are separated from humans by ~25 million years of evolution (Nei and Glazko, 2002), and exhibit major brain differences despite being members of the same primate order. Recent imaging studies have revealed substantial neuroanatomical differences between macaques and humans, for example in language-related connectivity and the proportion of cortex devoted to lightly myelinated association areas (Donahue et al., 2018; Glasser et al., 2014; Rilling et al., 2008). At the level of cortical areas, high confidence homologies suggestive of a common evolutionary origin have only been firmly established for a modest number of early sensory and motor areas (Van Essen and Dierker, 2007) but are more challenging to delineate for higher cognitive regions such as prefrontal cortex (Mars et al., 2018a, 2018b). Other outstanding questions may include: what is the optimal interspecies registration between macaque and human cerebral cortices? What are the optimal methods for non-invasively estimating functional and structural connectivity as assessed by comparison with gold standard invasive tracers in macaques? Which brain networks are shared and which are different between macaques and humans? These issues may benefit from improvements to in vivo neuroimaging acquisition and preprocessing.

Recently, the Human Connectome Project (HCP) developed an improved, integrated approach to brain imaging acquisition, analysis, and data sharing (Glasser et al., 2016b). The overall goal of this approach was to increase the sensitivity and precision with which brain imaging studies are conducted in the hope that this will yield results that are more neurobiologically interpretable and more accurately comparable across individuals and studies. The HCP-style approach has seven core tenets (Glasser et al., 2016b): 1) Acquire as much high-quality data from as many subjects as possible. 2) Acquire data with maximum feasible resolution in space and time 3) Preserve high data quality throughout preprocessing by removing physical distortions, subject movement within and between scans, image intensity inhomogeneities, and artefacts and nuisance signals without blurring the data or altering the neural signals (Andersson et al., 2003; Andersson and Sotiropoulos, 2016; Glasser et al., 2013, 2016b; 2018; Griffanti et al., 2014; Salimi-Khorshidi et al., 2014). 4) Use appropriate geometrical models—surfaces for the sheet-like cerebral cortex and volumes for globular subcortical structures (Glasser et al., 2013). 5) Perform alignment across subjects via cortical features, not cortical folds (Robinson et al., 2018, 2014). 6) Use a data-driven structurally and functionally sensible parcellation, ideally derived from multiple modalities (Glasser et al., 2016a). 7) Share results as data files in neuroimaging databases such as the Brain Analysis Library of Spatial maps and Atlases (BALSA) database (Van Essen et al., 2017), not just 3D coordinates. Following the HCP-Style approach in humans investigations led to dramatic improvements in spatial localization precision relative to traditional brain imaging methods (Coalson et al., 2018). Therefore, we sought to bring this improved brain imaging approach to non-human primate studies.

Monkey brains present distinct imaging-related challenges relative to human brains. The macaque brain is 10-fold smaller in weight, and its neocortex is ~25% thinner (average 2.0 mm vs 2.6 mm (Donahue et al., 2018; Glasser et al., 2016b)). These facts necessitate increased spatial resolution to achieve comparable neuroanatomical resolution; however, smaller voxels are associated with decreased signal-to-noise ratio (SNR). One way to improve SNR is to scan at ultrahigh magnetic field strength (e.g., 7T). However, ultra-high field scanners pose technical challenges such as increased B_0 and B_1 inhomogeneity (Van de Moortele et al., 2005). For conventional 3T scanners, one way to enable high-resolution whole-brain imaging in macaques is to optimize the multi-channel radiofrequency (RF) receiver coil. Using a coil matched to the macaque head size with a large number of small coil elements is predicted to improve SNR. Multi-channel signal acquisition using advanced 3T research scanners in humans enables parallel imaging both in the slice direction (i.e. multiband) (Moeller et al., 2010; Setsompop et al., 2012) and within the slice plane (generalized auto-calibrating partially parallel acquisitions [GRAPPA]) (Griswold et al., 2002). Although several studies have devised multichannel receive coils for macaque whole-brain imaging at 3T (Helms et al., 2013; Janssens et al., 2013; Khachaturian, 2010) and 7T (Gilbert et al., 2016; Gao et al., 2020), they have not to date demonstrated robust whole-brain mapping of multi-modal MRI measures such as those acquired by HCP. Achieving comparable results in macaques requires not only higher resolution and SNR but also low geometric distortion and signal intensity inhomogeneity, and requires optimized hardware, sequences, and post-processing techniques.

In this study, we designed and built a 24 channel receive coil with a geometry optimized for parallel imaging of anesthetized macaque monkeys and combined it with a 3T scanner with a high gradient (80 mT/m). Capitalizing on the accelerated imaging capabilities of the coil, we adapted HCP-style data acquisition protocols for structural MRI (Glasser et al., 2013), fMRI (Smith et al., 2013) and diffusion MRI (dMRI) (Sotiropoulos et al., 2013; Uğurbil et al., 2013) to the small size of the macaque brain, as well as the HCP-style minimal spatial preprocessing and denoising pipelines (Andersson and Sotiropoulos, 2016; Glasser et al., 2018, 2016a; 2013; Salimi-Khorshidi et al., 2014). We generate accurate white and pial cortical surfaces, subcortical segmentations, myelin maps, and cortical thickness maps from structural MRI, surface aligned fMRI dense timeseries that have spatial artefacts and nuisance signals removed, resting state functional networks, and diffusion-based fiber orientation estimates, example tractography connections, and cortical neurite orientation and dispersion imaging (NODDI) (Zhang et al., 2012). The spatial resolutions of the structural and functional imaging modalities are scaled to macaque cortical thickness, thus providing comparable neuroanatomical resolution to HCP-style human imaging and facilitating comparison of connectomes between macaques and humans.

2. Methods and materials

Experiments were performed using a 3T MRI scanner (MAGNETOM Prisma, Siemens, Erlangen, Germany) equipped with 80 mT/m gradients (XR 80/200 gradient system with slew rate 200 T/m/s) and a 2-channel B_1 transmit array (TimTX TrueForm). The animal experiments were conducted in accordance with the institutional guidelines for animal experiments, and animals were maintained and handled in accordance with the Guide for the Care and Use of Laboratory Animals of the Institute of Laboratory Animal Resources (ILAR; Washington, DC, USA). All animal procedures were approved by the Animal Care and Use Committee of the Kobe Institute of RIKEN (MA2008-03-11). We also used Young Adult HCP (YA-HCP) data as a reference for data quality. The use of YA-HCP data was approved by the institutional ethical committee (KOBE-IRB-16-24).

2.1. Macaque 24-channel coil

The coil frame geometry was designed using a 3D digital design software (Rhinoceros 5, McNeel, Seattle, USA) to closely fit the head of the animal with maximum head dimensions (anterior posterior 109 mm,

left-right 99 mm, superior-inferior 84 mm) (Fig. 1A) in our macaque head MRI database. The database included structural scans (T1w) of 133 individual subjects from three macaque species (*Macaca fuscata*, N = 4; *Macaca fascicularis*, N = 122; *Macaca mulatta*, N = 7; weight 2–8 kg). The largest animal's MRI data was used to delineate the contour of the head surface and imported into the 3D digital design software where the inner surface of the coil was designed to closely fit the head surface (Fig. 1A). 16 pentagonal and 8 hexagonal elements were configured over the surface (Fig. 1B), resembling a soccer-ball coil design (Wiggins et al., 2006). These elements were arranged in three quasi-horizontal arrays to maximize parallel encoding power of multiband EPI sequences for animals placed in the supine position and axial slices. The inner body of the device was constructed using a 3D printer (M200, Zortrax, Olsztyn, Poland) (Fig. 1C), and the coil elements were arranged over its external surface. Initially the coil elements were wired using a thin copper foil-plate (width 5 mm); however, because the plate elements markedly interfered with B_1 transmission (data not shown), the coil elements were rewired using thin coaxial copper cables (Fig. 1D, cable diameter 0.7 mm; cable loop maximum mean diameter 48.6 ± 8.7 mm) (Wiggins et al., 2009), which substantially reduced interference with B_1 transmission. The elements were arranged so as to continuously (critically) overlap each other thereby reducing coupling between nearest-neighbor coils. Coils in the caudal-posterior part were designed to have relatively larger diameter (35% larger in maximum diameter) to ensure increased sensitivity to distant brain regions (e.g. cerebellum) while reducing sensitivity to closer regions (e.g. occipital cortex). The two elements placed over the eyes were also relatively large in diameter to allow video recording of eyes and eyelids for monitoring depth of anesthesia. In addition, capacitors were arranged vertically against the surface of the coil frame to reduce interaction with B_1-transmission (Fig. 1D). Fig. 1E shows the circuits, which followed a standard design (Wiggins et al., 2006) consisting of diode detuning trap, cable trap and bias T connected to low input-impedance preamplifiers (Siemens Healthcare, Erlangen, Germany). The completed coil set up, in head-first supine position, on the scanner is shown in Fig. 1F.

2.2. Coil evaluation

Coil elements were assessed for the ratio of loaded to unloaded quality factor Q, nearest-neighbor coupling, and active detuning. Element coupling was estimated with gradient off-line noise correlation measurements. Two phantoms (NaCl 0.9%, gadolinium 0.1 mM) were designed and prepared using a 3D printer: one to closely match the inner-surface of the coil (Fig. 1G) used for B_1 quality evaluation and the other to match to a typical macaque brain size used for geometry-dependent noise amplification. B_1-transmission was assessed with a vendor provided flip-angle sequence. B_1-receive field was estimated using a gradient-echo sequence and by calculating the signal ratio between 24-channel and body receive coils. Finally, geometry-dependent noise amplification due to parallel imaging was evaluated using gradient-echo imaging and GeneRalized Autocalibrating Partial Parallel Acquisition (GRAPPA) (Griswold et al., 2002) in-plane acceleration factors of 2, 3 and 4.

2.3. Data acquisition strategy – resolution and contrast considerations

To improve comparability of macaque and human brains, our data acquisition strategy emulated methodologies introduced by the HCP (3T protocols) (Glasser et al., 2016b, 2013; Smith et al., 2013; Sotiropoulos et al., 2013; Uğurbil et al., 2013). To accurately model the cortical pial and white matter surfaces, structural imaging spatial resolution target

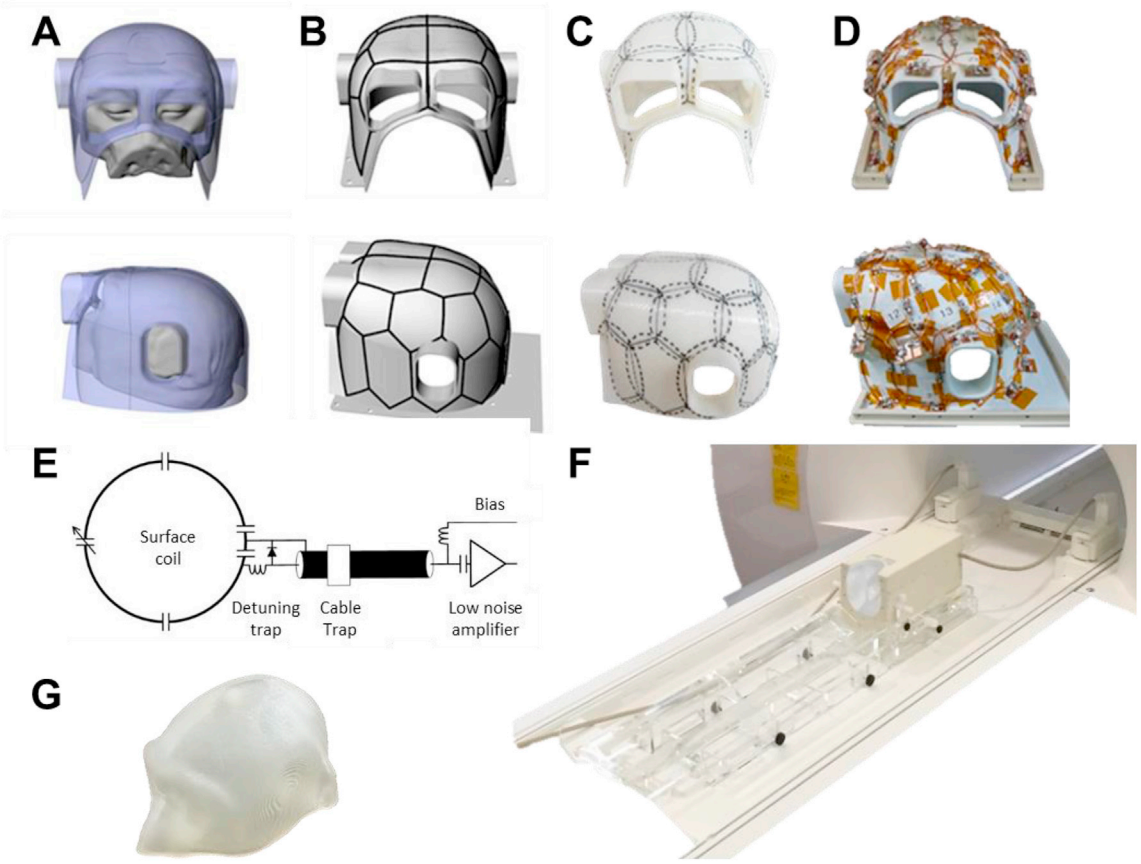

Fig. 1. The design and development of macaque 24-channel receive-only coil. (**A**) Design of coil geometry and **(B)** element locations. **(C)** Outlook of element alignment on a 3D print. **(D)** Coil with final element arrangements. **(D)** Schematic of a coil element circuit. (**E**) Coil circuitry. **(F)** Coil outlook with animal holder attached to the gantry of the MRI scanner. **(G)** Macaque head phantom.

(0.5 mm isotropic in macaques, equivalent to 0.8 mm in humans) was based on preliminary evaluations of macaque cortical thickness (Glasser et al., 2014) and corresponds to approximately half of the minimum cortical thickness in the cortex, which is ≈ 1 mm in macaques (Donahue et al., 2018) and 1.6 mm in humans (Glasser et al., 2016b). Tissue contrast (grey and white matter and CSF) associated imaging parameters (e.g. inversion time, flip angle, repetition time and echo-time) were experimentally adjusted to enable robust surface estimation within the FreeSurfer pipelines, in conjunction with maximizing intracortical T1w/T2w (myelin-related) contrast. The fMRI spatial resolution selection (1.25 mm) was based on preliminary evaluations of the 5th (low) percentile of cortical thickness, following a similar strategy to that in humans by the HCP (resolution of 2 mm) (Glasser et al., 2016b). The temporal sampling rate (TR = 0.75 s) was maximized according to tSNR (see below) which was close to the human protocol (0.72 s (Smith et al., 2013)). For dMRI, the smallest spatial resolution within the practical limitation of the SNR was chosen using the same b-value scheme (b = 1000, 2000 and 3000 s/mm^2) as in the HCP (Sotiropoulos et al., 2013) with 500 directions (more than the 270 in the HCP). Pilot studies for each modality included assessments for varying spatial resolution, flip-angle, RF transmission power, pulse length, inversion time (TI), fat suppression, multiband acceleration factor, in-plane acceleration factor, repetition time (TR), echo-time (TE), echo-spacing, spectral width, phase encoding direction, phase partial Fourier, phase oversampling, image resolution and diffusion directions. The key imaging parameters and features of the data acquisition are listed in Table 1 and are compared with those in publicly available macaque database (PRIMatE Data Exchange, PRIME-DE) (Milham et al., 2018) and in the YA-HCP protocol.

2.4. Structural acquisition protocol

T1w images were acquired using a 3D Magnetization Prepared Rapid Acquisition Gradient Echo (MPRAGE) (Mugler and Brookeman, 1990) sequence (0.5 mm isotropic, FOV = 128x128 × 112 mm, matrix = 256 × 256 slices per slab = 224, coronal orientation, readout direction of inferior (I) to superior (S), phase oversampling = 15%, averages = 3, TR = 2200 ms, TE = 2.2 ms, TI = 900 ms, flip-angle = 8.3°, bandwidth = 270 Hz/pixel, no fat suppression, GRAPPA = 2, turbo factor = 224 and pre-scan normalization). The value of TI (900 ms) was selected based on the contrast between white and grey matter and SNR. T2w images were acquired using a Sampling Perfection with Application optimized Contrast using different angle Evolutions (SPACE) sequence (Mugler et al., 2000) (0.5 mm isotropic, FOV = 128x128 × 112mm, matrix = 256 × 256, slice per slab = 224, coronal orientation, readout direction I to S, phase oversampling = 15%, TR = 3200 ms, TE = 562 ms, bandwidth = 723 Hz/pixel, no fat suppression, GRAPPA = 2, turbo factor = 314, echo train length = 1201 ms and pre-scan normalization). The total acquisition time for structural scans was 22 min (17 min for T1w and 5 min for T2w).

2.5. Functional acquisition protocol

To reduce susceptibility induced geometric distortions and signal loss, the data was acquired in LR and RL directions. Functional scans were acquired using gradient-echo EPI (FOV = 95 × 95 mm, matrix = 76 × 76, 1.25 mm isotropic, interleaved slice order, and number of slices = 45 covering the whole brain).

An empirical estimate of the effect of multiband slice acceleration factor on fMRI tSNR was obtained by a procedure similar to that used by the HCP (Smith et al., 2013). Briefly, simultaneous slice excitation enables a multiband factor fold reduction in the TR and subsequent incomplete T1-recovery leads to a reduction in the optimal (Ernst) flip angle and thus in tSNR. However, as more data volumes can be acquired in a matched time window, a more relevant estimate for the data quality can be calculated by multiplying the tSNR with the square root of acquired data timepoints. Therefore, tSNR was estimated with a matched image acquisition time (10 min) using a range of multiband factors (1, 3, 5, 6 and 8), minimum excitation and refocus RF-pulse lengths (with constant spectral width), TRs (3850, 1300, 840, 680 and 530 ms), corresponding (blood) Ernst angles (86, 65, 55, 51 and 45°) and a fixed bandwidth (1370 Hz/pixel).

These trials led us to select an acceleration of multiband factor = 5 with multiband LeakBlock kernel on (Cauley et al., 2014; Risk et al., 2018), and other imaging parameters of TR = 755 ms, number of slices = 45, flip-angle = 55°, TE = 30 ms, bandwidth = 1370 Hz/pixel and echo spacing = 0.95 ms, and pre-scan normalization for the fMRI data acquisition. To maintain the temporal autocorrelation structure of the data, long continuous runs were used (single-run scan time 51 min, 4096 frames, RL and LR directions resulting in a total acquisition time of 102 min).

Table 1
MRI scanning parameters and features of the current HCP-NHP macaque protocol in comparison with open macaque database (PRIME-DE) and Young Adult HCP (YA-HCP) protocols.

	HCP-NHP Macaque Protocol	Open Macaque Database (PRIME-DE)	**YA-HCP protocol**
MRI scanner			
Magnetic field strength (T)	3	3–7	3
Gradient performance (mT/m)	80	40–80	100
RF coil			
Number of channels	24[a]	4–24	32
Structural MRI			
Spatial resolution (mm)	0.5	0.3–0.5	0.7
T1w	Yes	Yes	Yes
T2w	Yes[a]	No, Yes	Yes
Functional MRI			
Spatial resolution (mm)	1.25[a]	1.4–1.65 at 3T 1–1.2 at 7T	2
Repetition time (s)	0.76[a]	1.6–2.0 at 3T 1.0 at 7T	0.72
Echo-time (ms)	30	16–30	33
Spin-echo fieldmap	Yes[a]	No	Yes
Gradient-echo fieldmap	No	No, Yes	No
In-plane acceleration	1	2 or NA	1
Cross-plane acceleration (multiband factor)	5[a]	1, 2, NA	8
Total scan time for resting-state fMRI (min/subject)	102[a]	13-476 (median = 41)	58
Total number of volumes for resting-state fMRI (volumes/subject)	8192[a]	500-13824 (median 1712)	4800
Diffusion MRI			
Spatial resolution (mm)	0.9[a]	1–1.4 at 3T 1.2 at 7T	1.25
Repetition time (s)	3.4	6.3–11.0 at 3T 3.8 at 7T	5.5
Echo-time (ms)	73	83-107 at 3T 54 at 7T	90
Number of b-shells	3[a]	1–3	3
b-value (mm^2/s)	1000-2000-3000[a]	1000, 1600, 1250–2500,850-1650-2500 at 3T, 1500 at 7T	1000-2000-3000
Number of diffusion gradient direction	500[a]	60, 80, 100, 120, 270	270
Opposing-phase encoding acquisition	Yes	No, Yes	Yes
In-plane acceleration	2	NA	1

[a] Imaging parameters that are important in the HCP-NHP protocol (left column) and were not often applied in PRIME-DE database (middle column). NA: not available.

2.6. Field-map acquisition protocol

The B_0 field-map was estimated using a pair of spin-echo EPI images with opposite phase encoding directions (Andersson et al., 2003) (LR and

RL directions, FOV = 95 × 95 mm, 1.25 mm isotropic resolution, axial orientation, slices = 45, interleaved data acquisition, TE = 46.2 ms, 6/8 phase partial Fourier, bandwidth = 1370 Hz/pixel, echo spacing = 0.95 ms, fat suppression and pre-scan normalization). The B_1 transmit field-map was obtained using vendor provided flip-angle sequence (Siemens, B_1-map) (FOV = 128x128 × 58mm, gap = 2 mm, gaps acquired in a separate run, 2 mm isotropic, TR = 10 s, target flip-angle = 90°).

2.7. Diffusion acquisition protocol

Diffusion scans were acquired with a 2D spin-echo EPI Stejskal-Tanner sequence (Stejskal and Tanner, 1965), utilizing monopolar gradient scheme and gradient pre-emphasis to reduce eddy currents. The monopolar gradients allowed decreased TE and significantly improved SNR without significant degradation due to eddy currents (in part due to the correction for eddy currents in post processing) (Andersson et al., 2003). The diffusion scheme contained three shells with b-values of 1000, 2000 and 3000 s/mm^2 (diffusion time = 26.5 ms, gradient duration = 17.8 ms and amplitude = 69.7 T/m), in accordance with the HCP (Sotiropoulos et al., 2013), but the number of direction (N_D) was increased to 500 uniformly distributed over the sphere, as compared with that in the HCP (N_D = 270). Furthermore, 52 b = 0 s/mm^2 volumes were evenly distributed across the diffusion scheme to reduce CSF pulsation related uncertainty in the b = 0 s/mm^2 image signal intensity. In contrast to the HCP, we used GRAPPA (acceleration factor = 2) to reduce image distortions and accelerate the sequence in plane with a more recent version of the multiband sequence than that which was available for the original young adult HCP (Uğurbil et al., 2013). In order to correct geometric distortions, the diffusion scheme was obtained using two scans with reversed phase encoding directions (LR and RL) and different number and directions of diffusion gradient (252 and 248) (Andersson and Sotiropoulos, 2016). The following imaging parameters were applied: FOV = 90 mm, matrix = 100 × 100, 0.9 mm isotropic resolution, number of slices = 60, interleaved slice acquisition, multiband factor = 2, multiband LeakBlock kernel on, GRAPPA = 2, TR = 3400 ms, flip-angle = 90, TE = 73 ms, 6/8 phase partial Fourier, echo spacing = 1.12 ms, bandwidth = 1086 Hz/pixel, pre-scan normalization on and fat suppression using gradient reversal technique (Gomori et al., 1988). Total acquisition time was 30 min, during which frequency drift was small (≈0.5 Hz/min). By applying slice and in-plane accelerations (2 × 2), the acquisition time was reduced by more than 3-fold compared to without acceleration. However, the shortest possible TR was not used, in order to preserve SNR (to allow near-complete longitudinal magnetization recovery).

2.8. Animal experiments

Macaque monkeys (mean 5.4 kg, range 3.0–8.8 kg, total N = 34; M.mulatta N = 16, M.fascicular N = 14, M.fuscata N = 4) were initially sedated with intramuscular injection of atropine sulphate (20 μg/kg), dexmedetomidine (4.5 μg/kg) and ketamine (6 mg/kg). A catheter was inserted into the caudal artery for blood-gas sampling, and endotracheal intubation (ID = 3.5 mm) was performed for steady controlled ventilation using an anesthetic ventilator (Cato, Drager, Germany). End-tidal carbon dioxide was monitored and used to adjust ventilation rate (0.2–0.3 Hz) and a tidal volume (10–20 mL/kg). After the animal was fixed in an animal holder, anesthesia was maintained using intravenous dexmedetomidine (DEX) (4.5 μg/kg/hr) and 0.6% isoflurane via a calibrated vaporizer with a mixture of air 0.75 L/min and O_2 0.1 L/min. The anesthesia protocol was based on literature on relative preservation of functional connectivity in DEX anesthesia in human (Guldenmund et al., 2017) and rodents (Pan et al., 2015). Compared with previous protocol of DEX in macaque (Zhao et al., 2015), we modified it to achieve a stable anesthetic condition with least adverse effect of cardio-suppression by DEX and higher resting-state BOLD activities than those in isoflurane-only (1.0%) anesthesia in preliminary studies. Animals were warmed with blanket and their rectal temperature (1030, SA Instruments Inc., NY, USA), peripheral oxygen saturation and heart rate (7500FO, NONIN Medical Inc., MN, USA) were monitored throughout experiments. For diffusion imaging the level of isoflurane was increased to 1.0% to reduce potential eye and head motion artefacts.

2.9. Data analysis

Data analysis utilized a version of the HCP pipelines customized specifically for use with non-human primates including structural (PreFreeSurfer, FreeSurferNHP (instead of FreeSurfer) and PostFreeSurfer), functional (fMRIVolume, fMRISurface) and diffusion preprocessing (Diffusion Preprocessing) (Donahue et al., 2016; Glasser et al., 2013) (for an overview flowchart, see Supplementary Fig. S1). The HCP-NHP pipelines require FMRB's Software Library (FSL) v6.0, FreeSurfer v5.3.0-HCP and Connectome Workbench v1.4.2 (https://www.humanconnectome.org/software/get-connectome-workbench) and are available at https://github.com/Washington-University/NHPPipelines.

2.10. Structural image processing

Preprocessing began with the PreFreeSurfer pipeline, in which structural T1w and T2w images were registered into an anterior-posterior commissural (AC-PC) alignment using a rigid body transformation, non-brain structures were removed, T2w and T1w images were aligned using boundary based registration (Greve and Fischl, 2009), and corrected for signal intensity inhomogeneity using B_1- bias field estimate. Next, data was transformed into a standard "Yerkes19_v1.2" macaque atlas (Donahue et al., 2018, 2016) by 12-parameter affine and nonlinear volume registration using FLIRT and FNIRT FSL tools (Jenkinson et al., 2002).

FreeSurferNHP pipeline was used to reconstruct the cortical surfaces using FreeSurfer v5.3.0-HCP (Fischl, 2012). This process included conversion of data in native AC-PC space to a 'fake' space with 1-mm isotropic resolution in volume with a matrix of 256 in all directions, intensity correction, segmentation of the brain into cortex and subcortical structures, reconstruction of the white and pial surfaces and estimation of cortical folding maps and thickness. The intensity correction was performed using FMRIB's Automated Segmentation Tool (FAST) (Zhang et al., 2001) followed by scaling the whole brain intensity by a species-specific factor (=80). This process significantly improved white and grey contrast particularly in the anterior temporal lobe as well as white surface estimation, an effect that may be associated with the so-called 'anterior temporal lobe problem' in pediatric brains, potentially due to less myelination in these white matter regions. We also improved the subcortical parcellation training dataset for the macaque brain (N = 21), and trained for 21 subcortical structures: brainstem plus bilateral accumbens, amygdala, caudate, claustrum (which is not a part of the default structures for human FreeSurfer), cerebellum, diencephalon, hippocampus, pallidum, putamen, and thalamus (Fischl, 2012). A training dataset for brain mask extraction was also created. After parcellating the cortical and subcortical structures with these training datasets using the T1w image, the claustrum was treated as putamen, so that subsequent white surface estimation accurately estimates the white surface beneath the insular cortex, as shown in the Results. The white matter segmentation was fine-tuned by filling a white matter skeleton to accurately estimate white surface around the blade-like thin white matter particularly in the anterior temporal and occipital lobe. After the white surface was estimated, the pial surface was initially estimated by using intensity normalized T1w image and then estimated using the T2w image to help exclude dura and blood vessels, as in the HCP pipeline (Glasser et al., 2013). We modified this procedure by applying an optimized value of maximal cortical thickness (=10 mm in 'fake' space, 5 mm in real space like the FreeSurfer default) and the average curvature (=25). The surface and volume data in 'fake' space was transformed back into the

native AC-PC space, and cortical thickness was recalculated in the animals' real physical space.

The PostFreeSurfer pipeline transformed anatomical volumes and cortical surfaces into the Yerkes19 standard space, performed surface registration using folding information via MSMSulc (Robinson et al., 2018, 2014), generated the mid-thickness surface (by averaging the white and pial surfaces), generated inflated and very inflated surfaces, as well as the myelin map from the T1w/T2w ratio on the mid-thickness surface. The volume to surface mapping of the T1w/T2w ratio was carried out using a 'myelin-style' mapping (Glasser and Van Essen, 2011), in which a cortical ribbon mask and a metric of cortical thickness were used, weighting voxels closer to the midthickness surface. Voxel weighting was done with a gaussian kernel of 2 mm FWHM, corresponding to the mean cortical thickness of macaque (see below). Surface models and data were resampled to a high-resolution 164k mesh (per hemisphere), as well as lower resolution meshes (32k and 10k) for processing diffusion and functional MRI data, respectively.

2.11. Functional data processing

Data were motion corrected, corrected for geometric B0-distortions using spin echo field-maps and TOPUP (Andersson et al., 2003) with adjusted warping resolution and smoothness, registered to the structural images using the single-band reference image and BBR (Greve and Fischl, 2009), normalized to grand 4D mean (=10000) and masked (Andersson et al., 2003; Gonzalez-Castillo et al., 2013; Smith et al., 2013). Intensity bias field correction was not carried out because the functional data were acquired with the pre-scan normalize filter on. The cerebral cortical grey matter voxels were mapped to the surface with the partial-volume weighted ribbon-constrained volume to surface mapping algorithm and voxels having large deviations (greater than 0.5 s.d. above mean) from the local (in a 5 mm sigma Gaussian) neighborhood voxels' coefficient of variation were excluded (Glasser et al., 2013). Data was minimally smoothed at 1.25 mm FWHM using geodesic Gaussian surface smoothing algorithm with vertex area correction and resampled according to the folding-based registration (MSMSulc) to a standard mesh in which the vertex numbers correspond to neuroanatomically matched locations across subjects. The subcortical grey matter voxels were processed in the volume using 1.25 mm FWHM subcortical parcel-constrained smoothing and resampling. Altogether, these processes transformed the functional data into a standard set of greyordinates (~10,000 [10k] vertices per hemisphere and ~8,000 [8k] subcortical voxels) using the Connectivity Informatics Technology Initiative (CIFTI) format (Glasser et al., 2013).

Structured temporal noise arising from imaging artefacts, motion and physiological noise was removed using a NHP version of FMRIB's ICA-based X-noisefier (FIX) ("sICA + FIX") (Glasser et al., 2018; Griffanti et al., 2017, 2014; Salimi-Khorshidi et al., 2014). Principal component analysis (PCA) was applied to segregate data into structured and unstructured sub-spaces and detect the dimensionality of the structured subspace based on comparison of the data eigenspectrum with a null data eigenspectrum (a Wishart distribution). The structured subspace was decomposed into statistically independent components using spatial ICA and the resulting components were manually classified as "signal" or "noise", based on their spatial distribution and temporal properties (Griffanti et al., 2017, 2014; McKeown et al., 1998). The FIX classifier was then trained on this manual classification (N = 30) and the performance level was characterized in terms of true positive rate (TPR) and true negative rate (TNR). A total of 186 spatio-temporal features were extracted including species-specific vein maps in the standard space and were used for training/classification. The performance of classifier was evaluated by leave-one-out (LOO) accuracy testing for a range of thresholds. Finally, unstructured noise was attenuated using a Wishart filter (Glasser et al., 2016a, 2016b) prior to dense connectome analyses.

Information about different categories of fMRI fluctuations were provided by HCP RestingStateStats (Marcus et al., 2013) adapted for monkey. In brief, RestingStateStats quantifies total fMRI variance (prior to any preprocessing) into six categories: high-pass filter, motion, artefacts and nuisance signals (by FIX classification), unstructured noise (by PCA, see above), neural blood oxygenation level dependent (BOLD) fluctuations (by FIX classification), and FIX-cleaned mean greyordinate timeseries (MGT). The fractional contribution of each category was calculated by dividing by the total fMRI variance.

2.12. Diffusion data processing

Following the HCP pipeline (Sotiropoulos et al., 2013), the diffusion data was normalized for mean intensity of the b = 0 volume, corrected for distortion using a spin-echo field-map (i.e. a pair of b = 0 volumes acquired in opposite phase), and for eddy-currents and motion using TOPUP and EDDY (Andersson et al., 2003; Andersson and Sotiropoulos, 2016). The images were subsequently registered to the T1w structural image using the undistorted b = 0 volume and a 6-DOF boundary-based registration (Greve and Fischl, 2009), transformed into 0.9 mm structural volume AC-PC space (spline interpolation), and masked with a brain mask. The diffusion gradient vectors were rotated according to the rotational information of the rigid transformation matrix from the b = 0 to T1w volume. The quality of the diffusion data was assessed using 'eddyqc' in FSL (Andersson and Sotiropoulos, 2015; Bastiani et al., 2019). Summary quality metrics consists of SNR calculated for the b = 0 volumes by average intensity divided by standard deviation of b = 0 volumes (n = 52), and for each b-value with diffusion angular CNR, i.e. the ratio between the standard deviation of the signal predicted by eddy using a Gaussian Process and the standard deviation of the residuals.

Fiber orientation estimation was performed with a model-based parametric deconvolution approach to estimate three crossing fibers per voxel using 'bedpostx_gpu' in FSL (Behrens et al., 2007; Hernández et al., 2013; Hernandez-Fernandez et al., 2018) with a burn in period of 3000 and a zeppelin deconvolution kernel (Jbabdi et al., 2012; Sotiropoulos et al., 2016). The uncertainty in the estimated fiber orientations in white matter voxels was compared with the respective uncertainty obtained when using HCP data, for each of three crossing fibers (orientations sorted based on identified volume fraction). Probabilistic tractography was performed on the fiber orientation estimates using FSL's 'probtrackx2_gpu' algorithm (Hernandez-Fernandez et al., 2018) to generate dense diffusion connectomes (Donahue et al., 2016). In brief, we used vertices in the white matter surface and voxels in the subcortical grey matter as a seed of tracking. Streamlines were allowed to propagate within subcortical regions, but were terminated on exit (Smith et al., 2012). The pial surface and a curvature threshold of 90° were used as stopping criteria. The brain mask calculated in FreeSurfer was used for a waypoint mask through which paths were maintained. The step length was set to 0.23 mm, one fourth of voxel size, and the maximum path length to 200 mm. The calculated dense connectomes were created by counting the number of streamlines that terminal on voxels within the seed regions and normalizing by the total number of generated streamlines. These dense connectomes were parcellated using a 91-area atlas (Markov et al., 2014) to reduce gyral bias and the parcellated connectome matrices were fractionally scaled, symmetrized, and $\log_{10}$-transformed (Donahue et al., 2016). The quality of the dMRI data and the success of the tracking algorithm were evaluated with respect to quantitative retrograde tracer data by correlating $\log_{10}$-transformed tractography with the corresponding $\log_{10}$-scaled fraction of labeled neurons in a source area relative to the total number of label neurons extrinsic to the injected area (FLNe) (Donahue et al., 2016; Markov et al., 2014). The 91 area atlas allowed extraction of a 29×91 weighted and directed matrix with full information on a 29×29 subgraph. These graphs were used for further correlating those between tracer weights obtained from animals (N = 28) (Donahue et al., 2016; Markov et al., 2014) and diffusion tractography weights averaged across animals (N = 15). We analyzed connection lengths estimated by tractography streamlines and weighted average in each parcel (Donahue et al., 2016).

Neurite orientation dispersion and density imaging (NODDI) was used to evaluate tissue microstructure associated with neurite composition (a collective term referring to both dendrites and axons) (Zhang et al., 2012). Briefly, NODDI models three compartments (intra-cellular, extra-cellular and CSF) each with different diffusion properties (stick--tensor-ball model), where the diffusion motion in the intra-cellular compartment is assumed to be restricted to within neurites (stick), while that in the extra-cellular compartment is assumed to be a combination of Gaussian anisotropic (tensor) hindered by the presence of neurites, and Gaussian isotropic (ball) in CSF. The model includes two *a priori* assumed parameters of intrinsic axial diffusivity 1.1 μm^2/ms optimized for grey matter (Fukutomi et al., 2018), and isotropic diffusivity 3.0 μm^2/ms (Zhang et al., 2012), as well as four unknown parameters (intra-cellular volume fraction, concentration parameter of Watson distribution (K), mean orientation of Watson distribution (μ) and isotropic volume fraction (V_{iso}). The estimated parameters of orientation dispersion index (ODI) and neurite density index (NDI), as well as diffusion tensor parameters of fractional anisotropy (FA) and mean diffusivity (MD), were mapped onto the cortical surface using an algorithm weighted towards the cortical mid-thickness (Fukutomi et al., 2018).

3. Results

3.1. Coil performance

Coil bench tests showed that the unloaded/loaded Q ratio of the individual coil elements were approximately 215/75 = 2.9. This relatively low Q-ratio results from the small degree of loading and small electromagnetic flux due to the small diameter of the coil elements. Decoupling between adjacent elements was less than −20 dB indicating low mutual inductance between the elements. This produced noise correlation coefficients averaging 0.084 (interquartile range 0.02 and 0.126) with a maximum of 0.395 (see correlation matrix Fig. 2A). High noise correlation was largely constrained to the nearest neighbor elements (see Fig. 1B for element geometry, see also Supplementary Fig. S2 for coil channel-specific noise correlation maps).

The inverse g-factor map, a measure of coil element separation, illustrates geometry dependent signal intensity variation due to parallel image reconstruction used for dMRI (Fig. 2C). A reduction factor of two yields an average inverse g-ratio slightly larger than unity (1/g = 1.03 ± 0.07; values reported throughout text as mean ± s.d. unless otherwise specified), indicating a small noise cancellation attributable to low element noise correlation and parallel image reconstruction. However, larger reduction factors (R = 3 and 4) yield substantial degradation of signal intensity depending on geometry (Fig. 2C and D), suggesting that a maximum GRAPPA of 2 is practical for this coil.

3.2. Macaque data quality evaluation

Structural bias-field corrected T1w and T2w weighted images acquired at 500-μm resolution are shown in Fig. 3A and B, respectively.

Flip-angle maps indicate that the transmission was slightly higher in subcortical regions compared to cortical structures (Fig. 3C), as expected. However, the surface map (Fig. 3D) indicates that the RF transmission was relatively uniform over the cortical surface (86.6° ± 2.3) (see also Supplementary Fig. S3A for phantom data). Thus, signal intensity and contrast variations across the macaque cortical grey matter sheet attributable to RF-transmission inhomogeneity are modest for this coil.

B_0 volume (Fig. 3E) and surface (Fig. 3F) maps show inhomogeneities, particularly in and near air cavities adjacent to the cerebellum and inferior temporal cortex. These inhomogeneities cause signal intensity loss and spatial distortion in gradient-echo EPI images. Representative tSNR volume (Fig. 3G) and surface (Fig. 3H) maps, acquired with EPI at 1.25 mm isotropic resolution, provide a quantitative indicator of fMRI data quality. The mean FIX-cleaned tSNR in the macaque brain was 51.6 ± 25.6 overall, 67.5 ± 23.7 in the cortical ribbon and 37.3 ± 14.1 in subcortical regions. These macaque tSNR values are higher than for YA-HCP data: the FIX-cleaned tSNR in an exemplar HCP subject was 38.1 ± 15.1 in the whole brain, 43.0 ± 15.2 in the cortical ribbon, and 30.7 ± 10.8 in subcortical regions (Supplementary Fig. S4 and Table S1). However, a relatively low cortical tSNR in lateral occipito-

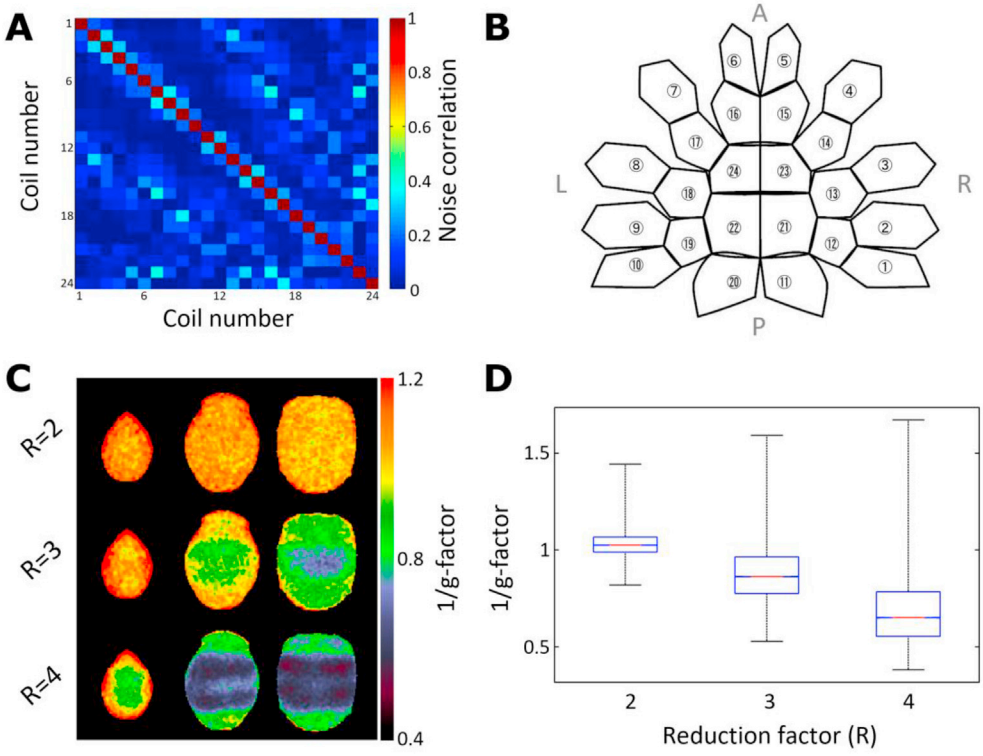

Fig. 2. Macaque 24-channel coil performance and geometry. **(A)** Noise correlation matrix. **(B)** Coil element arrangement and labeling flattened into a 2D representation. **(C)** Inverse geometry (1/g)-factor maps using gradient echo imaging with generalized autocalibrating partially parallel acquisitions (GRAPPA) reduction factors (R = 2, 3 and 4) in LR-direction used for diffusion MRI (see later). **(D)** The boxplot shows 1/g-factor with respect to reduction factor. While geometric distortions are small with acceleration factor of 2 (1/g = 1.03 ± 0.07), further reduction yields large signal degradations. Geometric distortions were evaluated using a phantom whose contour was matched to the average macaque brain.

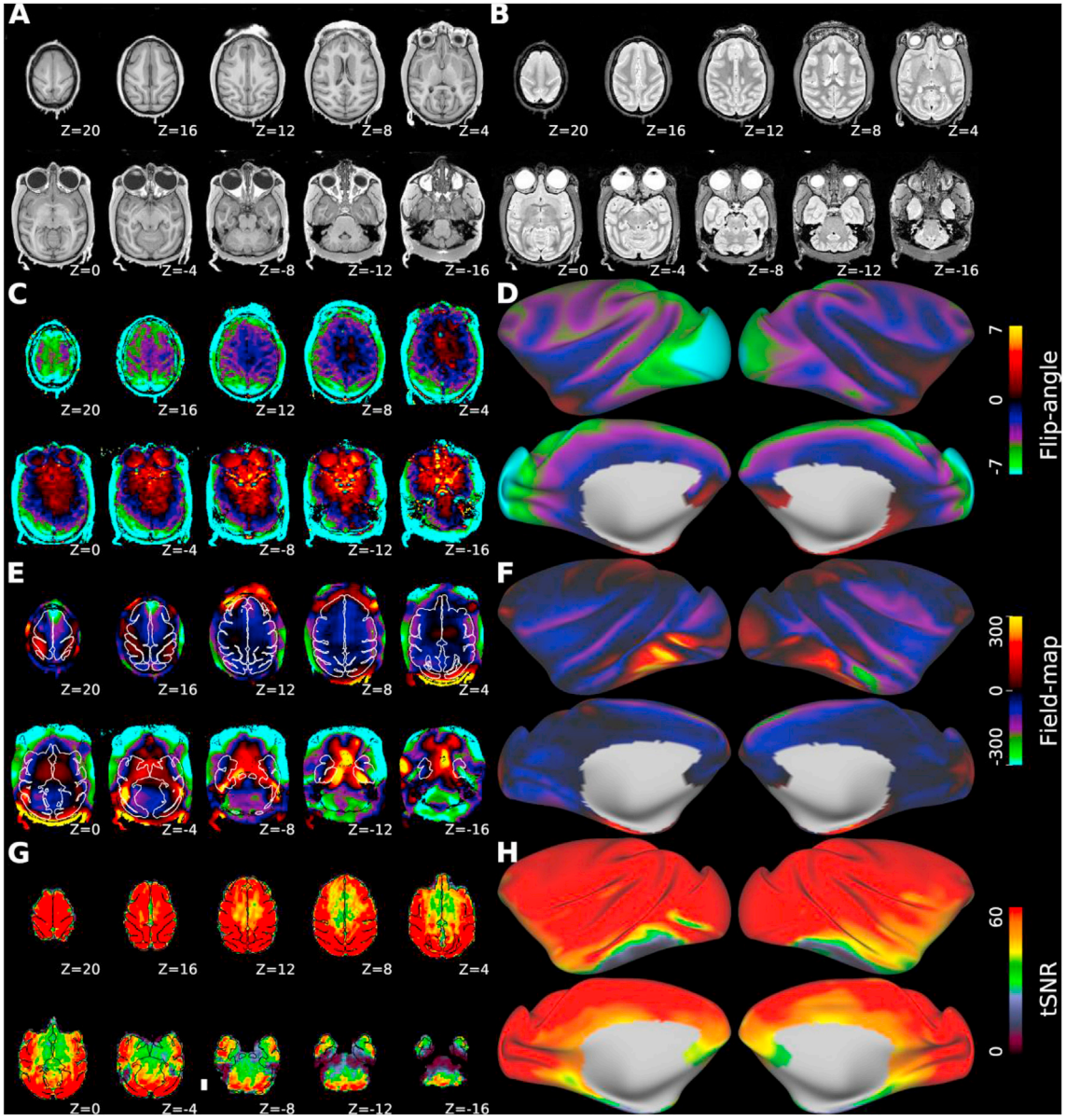

Fig. 3. Data quality assessment of structural and functional MRI. Axial slices acquired with 500 μm isotropic resolution **(A)** T1-weighted MPRAGE and **(B)** T2-weighted SPACE. Flip-angle **(C)** axial and **(D)** surface maps. The values indicate the difference between experimental and nominal flip-angle (90°) in units of degree. B_0 **(E)** axial and **(F)** surface field-maps. Unit radian per second. White and black lines (in E and G, respectively) outline the pial surface. Temporal signal-to-noise ratio (tSNR) **(G)** axial and **(H)** surface maps of FIX-cleaned fMRI. The tSNR map was acquired using multiband 2D-EPI sequence (TR = 0.755s, TE = 30 ms, MBF = 5, isotropic resolution = 1.25 mm). Data at https://balsa.wustl.edu/Z44X3.

temporal cortex is notable in the macaque data (Fig. 3H), which is mainly attributable to a large B_0 dephasing effect (Fig. 3F).

3.3. *Single-subject cortical architecture in three macaque species*

FreeSurfer automated segmentation of cortical and subcortical structures using our HCP-NHP structural pipeline was reliable across subjects (Supplementary Fig. S5B) and benefited from additional signal intensity normalization (Supplementary Fig. S5A, see also Supplementary Fig. S3A and S3B for B_1-transmit and receive fields, respectively). Inspection of pial and white matter surface contours indicates that the automatic segmentation generally followed the contrast boundaries of the T1w image (Supplementary Fig. S5C) and the T2w image (Supplementary Fig. S5D) appropriately, including in challenging thin heavily myelinated regions such as early visual and somatosensory cortex. The subcortical structures including claustrum, pallidum, putamen, were automatically and accurately segmented by the improved subcortical atlas (Supplementary Fig. S5B). The newly added intensity normalization improved the problematic estimation of the white matter surface in the anterior temporal lobe (Supplementary Fig. S6A right), which was not achieved using the default intensity bias field correction (Supplementary Fig. S6A left). The claustrum parcellation strategy also improved the white matter surface just beneath the insular cortex (Supplementary Fig. S6B, right), which often resulted in 'claustrum invagination' of the white surface by the default FreeSurfer (Supplementary Fig. S6B left). The claustrum parcellation also improved myelin contrast in the anterior insular area (see next paragraph).

Fig. 4 shows representative cortical surface mapping for three macaque species: Japanese rhesus monkey (*M. fuscata*), rhesus monkey (*M. mulatta*) and crab-eating monkey (*M. fascicularis*), as well as for average of three species (N = 12, consisting of N = 4 for each species). Although the brain size and surface area were different across species and

individuals, we successfully achieved cortical and subcortical parcellation by applying the same Gaussian Classifier Atlas (GCA) and obtained the surface estimation on gyral and sulcal formations (Fig. 4A–H), myelin contrast (Fig. 4I-L), which were comparable across species. The total cortical surface area per hemisphere (excluding the non-cortical 'medial wall') ranged from 8,093 to 12,897 mm^2 with an average of 10,052 ± 1,584 mm^2 (number of hemispheres = 24). The average myelin map (Fig. 4L) showed relatively high values in primary visual, sensorimotor and auditory regions and in the "MT+" complex, whereas association areas show relatively low values. These results for myelin maps are in good agreement with each other and with published group average macaque maps (Donahue et al., 2018; Glasser et al., 2014; Glasser and Van Essen, 2011). However, the myelin level in anterior insular cortex tended to be low relative to these earlier maps (Glasser et al., 2014); we consider the present maps likely to be more accurate since this region of agranular insular cortex is very lightly myelinated (Mesulam and Mufson, 1982). Our maps likely benefitted from improved segmentation between claustrum and insular cortex, as described above.

Cortical thickness maps were reasonably consistent across three macaque species (Fig. 4M–P). Most of frontal, anterior insular and temporal cortices are relatively thick, whereas most of visual and parietal cortices are relatively thin. Histograms indicate the distribution of cortical thickness (Fig. 4Q–T). Average cortical thickness was similar across species (M.fuscata mean 2.0 ± 0.2 mm, N = 4; M.mulatta mean 2.1 ± 0.1 mm, N = 4; M.fascicularis mean 2.2 ± 0.1 mm, N = 4), and average across animals was 2.1 ± 0.2 (median 2.0 mm, N = 12). The (lower) fifth

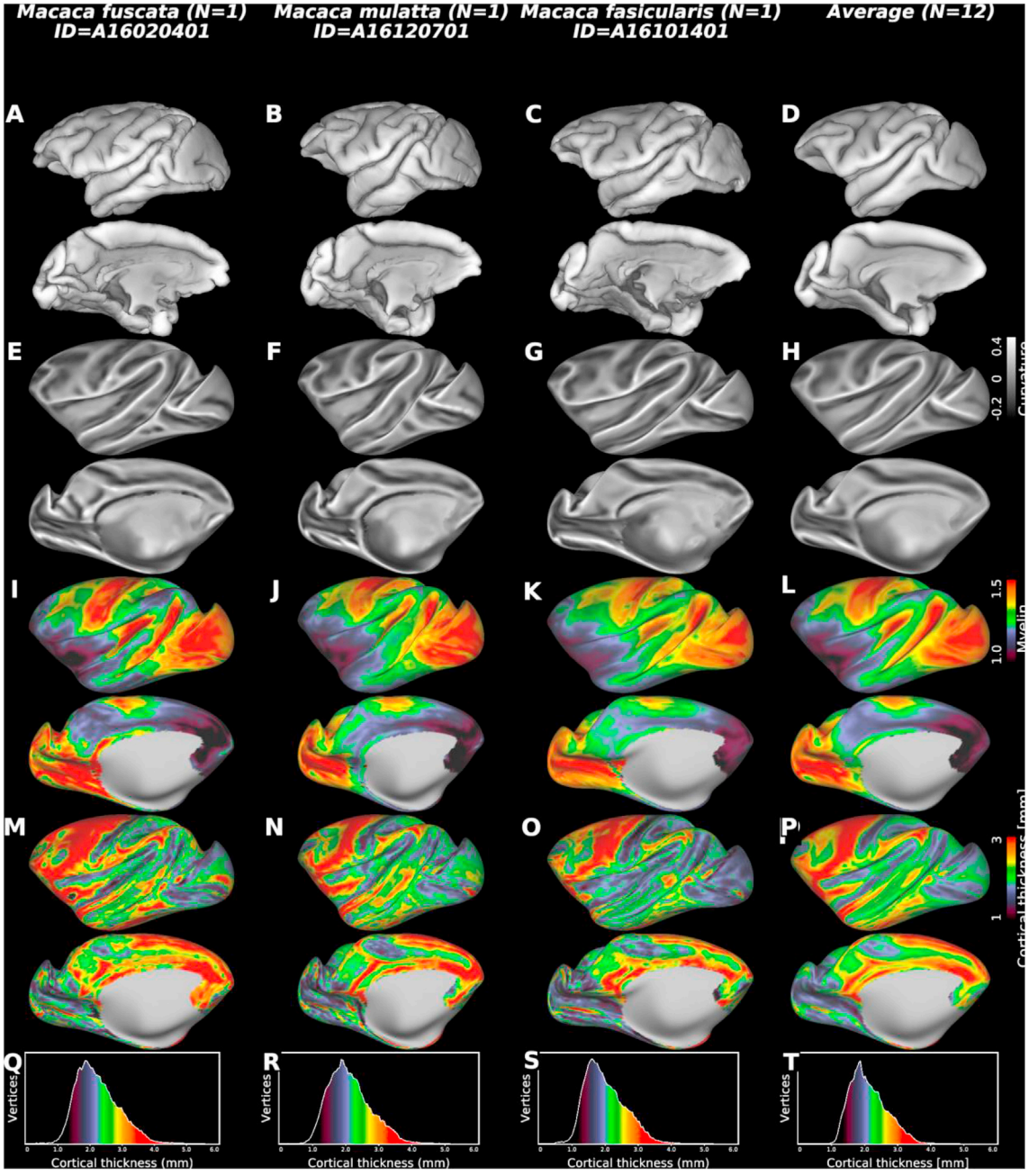

Fig. 4. Cortical surface mapping of three widely studied macaque monkeys. Japanese rhesus (*Macaca fuscata*, N = 1), rhesus (*Macaca mulatta*, N = 1), and crab-eating monkey (*Macaca fascicularis*, N = 1) and average maps across the species (N = 12; N = 4 for each species). **(A, B, C, D)** Pial surface. **(E, F, G, H)** Curvature and **(I, J, K, L)** bias-corrected myelin maps shown on very inflated cortical surface. Cortical thickness **(M, N, O, P)** maps and (**Q**, **R**, **S**, **T**) histograms. Data at https://balsa.wustl.edu/VjjZV.

percentile of the cortical thickness, evaluated from species average, was 1.38 mm. These estimates indicate that utilizing rfMRI isotropic resolution of 1.25 mm (≈2 mm^3) can capture voxels mainly within the cortical sheet, with modest partial volume effects. Of note, the gyral/sulcul patterns were very similar among these three macaque species. The cross-species variability of sulcal depth (average of sulc standard deviation = 0.12 in MSMSulc) did not differ from those within each species (0.11 in *M. mulatta*, 0.10 in M.fascicularis 0.10 in M.fascata), and were notably smaller than in human (0.35 in HCP MSMAll, N = 505).

3.4. Data quality of resting-state fMRI

To estimate the optimum multiband factor in fMRI, we determined the relationship between tSNR × sqrt(timepoints) and multiband acceleration factor (Fig. 5A) and found that tSNR × sqrt (timepoints) increases up to a factor of 5, then decreases. This trend was more evident after the data was processed using ICA-based artefact removal algorithm FIX, which yielded approximately 25% improvement in tSNR. In the cortical ribbon, denoised tSNR × sqrt (timepoints) is clearly highest at MBF = 5 (Fig. 5B).

The resting-state fMRI runs were analyzed using single-run sICA + FIX. The resulting sICA components (a total of number of components: 124 ± 29 for each animal, N = 30) were manually classified as noise (on average 100 ± 23 components per animal) or signal (22 ± 9 components per animal). The manual classification worked well to train FIX, and the classification accuracy achieved reasonably high performance (Table 2). The LOO accuracy testing showed that mean TPR and TNR ranged between 98.1-99.9% and 94.1–99.5%, respectively, depending on the choice of threshold. A threshold of 20 was used for classification, which resulted in mean TPR and TNR of 99.5% and 98.6%.

Using RestingStateStats in HCP Pipeline (Glasser et al., 2018; Marcus et al., 2013), the variance in macaque resting-state fMRI runs was divided into six categories. Fig. 6 shows their relative contributions to the total signal variance (38,400 ± 13,000, N = 20, see also Supplementary Table S2). Relative variance estimations in descending order were unstructured noise (70.0 ± 4.8%), high-pass filtered noise (15.3 ± 4.5%), structured noise (i.e. artefacts and nuisance signals, 6.0 ± 1.5%), (neural) BOLD fluctuations (4.1 ± 2.3%), motion (2.9 ± 1.3%), and FIX-denoised global signal timeseries (1.0 ± 0.7%). In comparison to HCP, unstructured noise accounted for a slightly larger portion in macaque (Fig. 6), which mainly originates from subcortical structures (see Supplementary Fig. S7 for spatial distribution of the variance categories). Furthermore, the relative BOLD contribution was smaller in macaque (4.1%) in comparison to HCP (7.7 ± 2.6%). Taken together, the contrast-to-noise ratio (CNR), defined as ratio between BOLD and unstructured signal, was smaller in macaque (0.21 ± 0.07) than in HCP (0.37 ± 0.08), which might be due to reduced BOLD signals in the anesthetized state (see section Resting-state fMRI in Discussion).

Table 2
FIX classification accuracy tested by leave-one-out (LOO) in thirty anesthetized macaque data. Abbreviations: TPR = true positive rate of signal components and TNR = true negative rate of true artefact components.

FIX threshold	1	2	5	10	20	30	40	50
TPR (mean)	99.9	99.9	99.5	99.5	99.5	99.0	98.6	98.1
TNR (mean)	94.1	95.9	97.5	98.1	98.6	99.0	99.4	99.5
TPR (median)	100	100	100	100	100	100	100	100
TNR (median)	95.5	96.6	97.7	98.2	98.7	100	100	100

One useful way to inspect the data quality is to visualize global (and semiglobal) artefacts in a 2-dimensional heatmap with time on the x-axis and parcel (M132) timeseries on the y-axis (i.e. greyplot) (Glasser et al., 2018; Power, 2016; Power et al., 2014). Comparison of a representative greyplot prior to any preprocessing (Supplementary Fig. S8A) and after preprocessing (Supplementary Fig. S8B) demonstrated that preprocessing reduced structured artefacts. MGT also demonstrate that FIX reduced the global signal variance, which in humans is primarily related to respiration after removal of movement artefacts by sICA + FIX. MGT power spectrum (Supplementary Fig. S8C) revealed distinct peaks within the ventilation frequency range (0.25–0.30 Hz). Preprocessing effectively attenuated ventilation artefacts, but only partially attenuated the low frequency, more likely neural, fluctuations (<0.1 Hz). Across subjects, the MGT variance was 2,230 ± 1,530 prior to preprocessing and 170 ± 110 after preprocessing (Supplementary Fig. S8D, N = 20). There appears to be relatively less global physiological noise in the macaque data relative to the human data (Glasser et al., 2018; Power, 2016), perhaps because the animals' respiration was externally controlled by the respirator.

Fig. 7 shows a representative resting-state network (RSN) component and seed-based connectivity obtained in a single monkey. Data was from two 51-min fMRI scans, preprocessed for correction of motion, distortion, inhomogeneity, and denoising with multi-run FIX as described above. The dense timeseries was further reduced in random noise using Wishart filtering (Glasser et al., 2016a) and was used for seed-based dense connectivity by computing the full correlation. The example RSN component (Fig. 7A) extended positive connectivity over posterior parietal cortex (areas 7A, DP, LIP), precuneus (areas 23, 31), temporo-occipital areas (MST, PGa) and prefrontal cortex (areas 46d, 8b). Temporal properties of this component included low frequency fluctuations, less than 0.2 Hz, which are typical of RSNs. A similar functional connectivity pattern was found using a single greyordinate seed placed over area 7A (Fig. 7B). Both the RSN signal components (a total of 32 signals) and the dense functional connectome can be interactively viewed in Connectome Workbench after downloading data from the BALSA database (https://balsa.wustl.edu/3ggwG). Overall, these results demonstrate that our experimental setup enables robust functional connectivity detection and analysis.

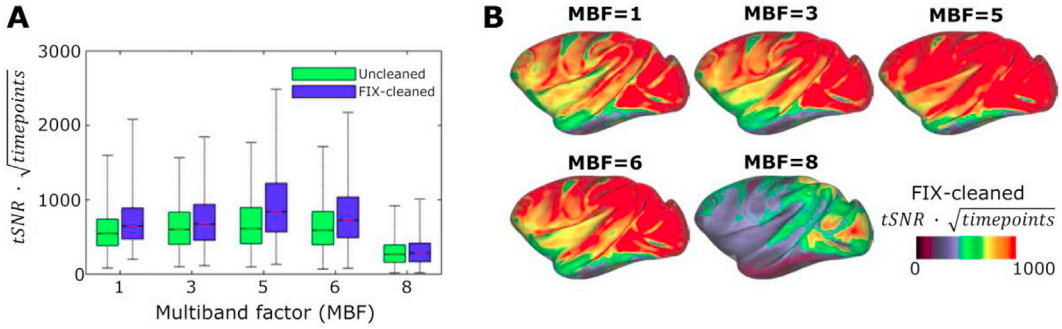

Fig. 5. Optimization of fMRI multiband acceleration. **(A)** Relationship between temporal signal-to-noise ratio (tSNR) multiplied by a square-root of acquired timepoints and multiband factor (MBF). Acquisition times are matched in the data points (each scan 10 min, N = 1). The boxplot shows distributions of tSNR in the greyordinates (a total of 26k) for FIX-uncleaned (green) and FIX-cleaned data (blue). **(B)** Cortical surface presentation of FIX cleaned tSNR × sqrt (#timepoints) vs multiband factor. Note that MBF = 5 produces the highest tSNR.

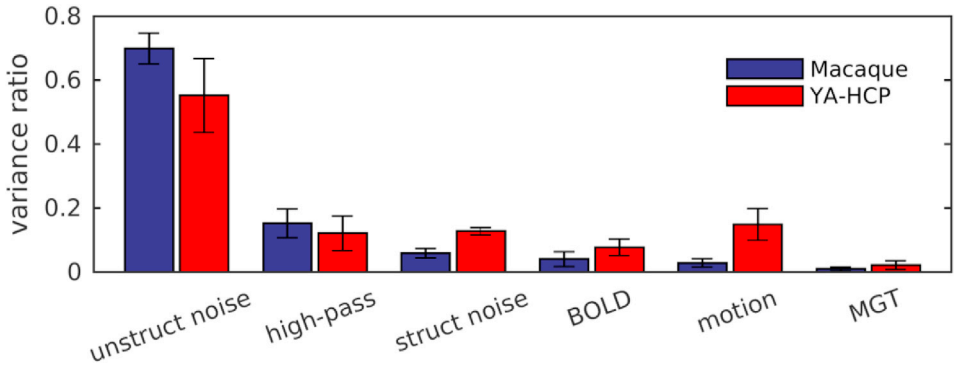

Fig. 6. Classification of resting-state fMRI variance and their relative contributions of the total variance in macaque (N = 20) and the young-adult human connectome project (YA-HCP, N = 20). The variances were computed using a development version of the Resting State Stats HCP pipeline. Abbreviations: struct noise = structured noise (scanner artefacts and nuisance signals etc.), BOLD = 'neural' blood oxygen level dependent signal, MGT = FIX-cleaned mean greyordinate timeseries.

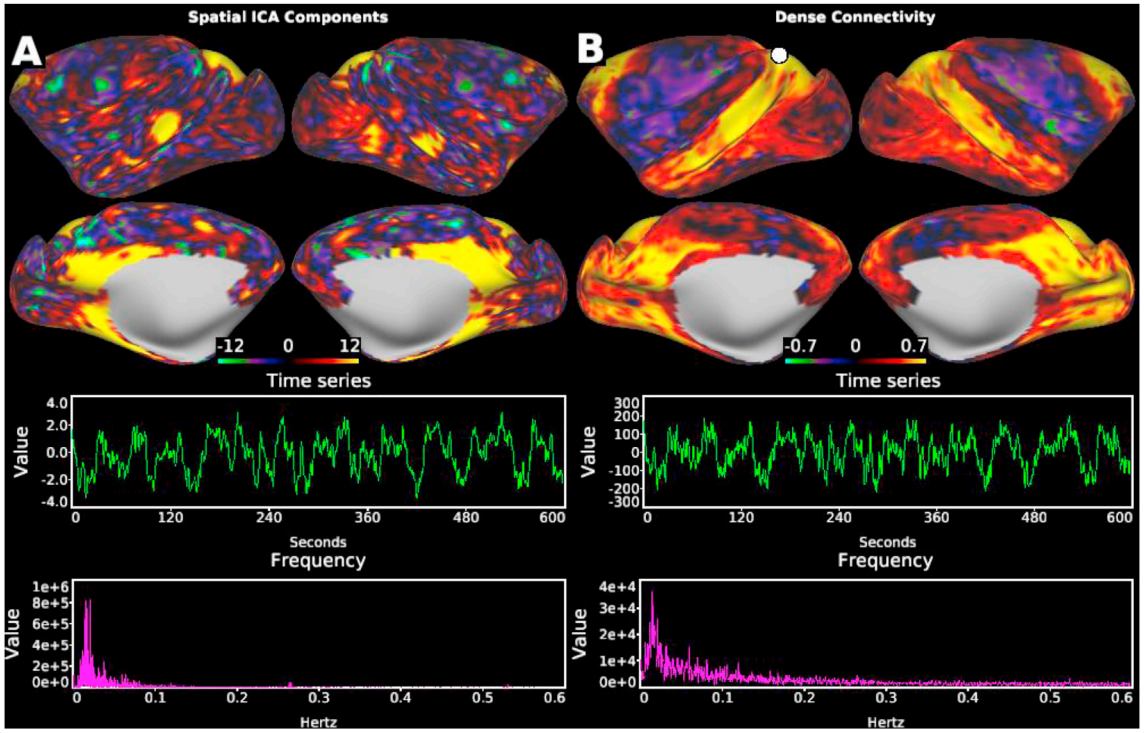

Fig. 7. Representative macaque resting-state functional connectivity in a single subject. **(A)** An example resting-state network (RSN) obtained in spatial ICA (unitless), which shows positive connectivity over posterior parietal cortex (areas 7A, DP, LIP), precuneus (areas 23, 31), temporo-occipital areas (MST, PGa) and prefrontal cortex (areas 46d, 8b, as defined in M132 atlas). Timeseries and frequency of this component (lower panels) exhibited pronounced hemodynamic-like low-frequency oscillations. (**B**) Exemplar functional connectivity seeded from a single greyordinate in area 7A (white circle). Spatial distribution of connectivity resembled to that of the component in (A), as well as timeseries and frequency of the seed signal (lower panels). Data was from two 51-min fMRI scans (subject N = 1), preprocessed for correction of motion, distortion, inhomogeneity, and denoising with multi-run FIX. The dense timeseries was further reduced in random noise by Wishart filter and used for seed-based dense connectivity. The colorbar indicates Pearson's correlation coefficient. Other components classified into signal or noise, and dense connectivity seeded from other vertices can be interactively viewed using Workbench using data at https://balsa.wustl.edu/3ggwG.

3.5. Diffusion MRI

Following the HCP paradigm, we used reversed left-right phase-encoding directions in dMRI acquisition to reduce TE, TR and distortion and to increase SNR and angular CNR. An example of image distortion and correction (axial and coronal views) is shown in Supplementary Fig. S9. Image distortions are large near regions with large B_0 inhomogeneity (i.e. temporal lobe, see Fig. 3E and F). Nonetheless, distortion correction was accurate, albeit with some signal drop-out and degraded SNR in these regions. Mean motion absolute displacement during 30-min acquisition was 0.36 ± 0.07 mm (N = 10), ensuring little interaction between head motion, eddy-currents and changes in static magnetic field. In contrast to HCP at 3T (Uğurbil et al., 2013), we used simultaneous MB and GRAPPA acceleration to reduce distortions. Inspection of temporal stability of the dMRI acquisition did not reveal pronounced structural artefacts around the ventricles and basal slices (Supplementary Fig. S10), thus indicating that simultaneous MB and GRAPPA accelerations did not substantially interact with physiological noise (Uğurbil et al., 2013). The dMRI quality assurance measures were similar between this study and the HCP (Fig. 8). Average SNR (whole brain) was 11.6 ± 1.4 in macaque (N = 10) and 9.4 ± 0.9 in the HCP (N = 10) (Fig. 8A). Exemplar subject data are compared in Supplementary Fig. S11 and Supplementary Table S3. The CNR slightly increased towards higher b-values and was similar across studies (Fig. 8B). In white

matter, three crossing fibers voxels (selected by thresholding at 0.05 of third fiber's volume fraction) were detected in 59% ± 7% and 57% ± 4% of voxels in macaque and the HCP, respectively (Fig. 9D). Finally, the dispersion uncertainties of 1st, 2nd and 3rd fiber orientations these voxels exhibited were also similar across the studies (Fig. 9E).

Fig. 9 shows M132 parcellated cortical maps of MD (Fig. 9A), FA (Fig. 9B), NDI (Fig. 9C) and ODI (Fig. 9D) (N = 6). The MD is low in the primary motor (F1) and premotor cortices (such as F2, F4, F5), and primary sensory cortices including somatosensory (areas 3, 1, 2), visual (V1) and auditory cortices including core, as well as intraparietal sulcus area (Fig. 9A), whereas the NDI is high in all of these areas. MD and NDI were strongly anti-correlated ($R = -0.75$, $p < 0.001$). The ODI was high in the periphery of the V1, somatosensory area 1, auditory cortices including core (Fig. 9D) and intermediate in MT and other higher visual areas. The FA was higher in the frontal and anterior temporal cortices and strongly anti-correlated with ODI ($R = -0.86$, $p < 0.001$). These results are comparable with those observed in the HCP (Fukutomi et al., 2018, 2019). The structural connectivity patterns extracted from diffusion tractography (DT) were also parcellated and explored with respect to the published quantitative retrograde tracer data (Fig. 9E and F) (Markov et al., 2014). Comparison of F5-seed connectivity between parcellated DT (pDT) and tracer data (in the 29x 91 matrix) showed a relatively good correlation (Spearman's $R = 0.62$, $p < 0.001$, for edges with tracer connectivity weight larger than 10^{-6}: N = 72). However, the fidelity of pDT decreased for weak long-distance connections (e.g. false positive connection to MT and MST and false negative connections to V2, V3, TEpd and TEpv), as reported previously (Donahue et al., 2016). Analysis of the bidirectional connectivity matrix (29 parcels × 29 parcels) of the pDT (N = 15) as in the tracer (N = 28) (Fig. 9G), gave correlation coefficients of connectivity weights between pDT and tracer of 0.56 (including all the edges: n = 406) and 0.57 (using edges with tracer connectivity weight larger than 10^{-6}: n = 322) (Fig. 9H), which were comparable with those between the ex-vivo pDT and tracer (0.55 and 0.56 respectively) (Donahue et al., 2016). At the single subject level, average pDT vs tracer correlation coefficient was 0.54 (max 0.59, min 0.48; including all the 406 edges) and 0.51 (max 0.58, min 0.41; using edges > 10^{-6}).

4. Discussion

Here, we have presented an adaptation of the HCP's approach to multimodal MRI acquisition, preprocessing, and analysis to the macaque, using the combination of a custom-made 24-channel receive-coil, high-resolution parallel imaging, and the HCP-NHP preprocessing and analysis pipelines. This approach yields robust estimates of cortical thickness, myelin content, and functional and diffusion measures. Importantly, since the presented protocols used share similar strengths to the HCP image acquisition, and the data is stored in a common geometrical framework system ('CIFTI greyordinates'), we anticipate that it will facilitate direct multi-modal comparisons with an unprecedented accuracy between macaque and human connectomes. To enable other groups to do HCP-Style analyses in the macaque, this 24-channel macaque coil is available (via Rogue Research, Montreal, Canada; produced by Takashima Seisakusho Co. Ltd., Tokyo, Japan) and the data acquisition protocols (including animal management and MRI scanning) are freely available from our website (https://brainminds-beyond.riken.jp/hcp-nhp-protocol), enabling other investigators to adapt, compare and make the best use of the parallel imaging capabilities of the coil. The HCP-NHP analysis pipelines are also available on github (https://github.com/Washington-University/NHPPipelines) along with macaque specific FIX training file and datasets on the website of FSL-FIX (https://www.fmrib.ox.ac.uk/datasets/FIX-training/).

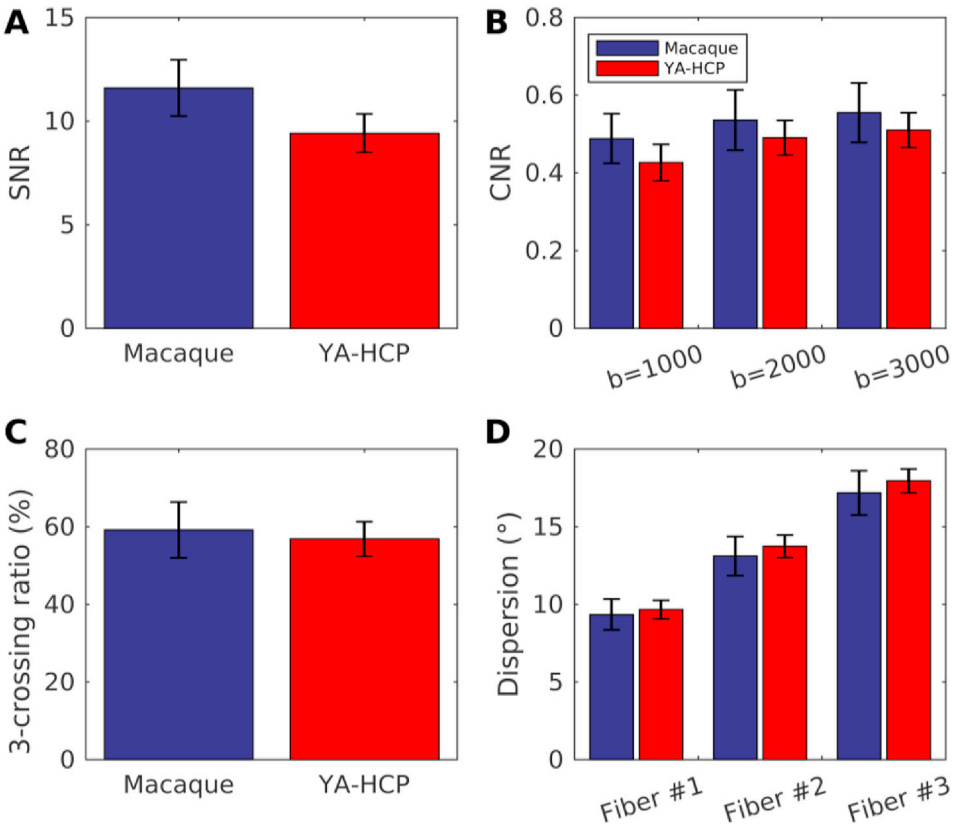

Fig. 8. Comparison of dMRI quality measures between macaque and the YA-HCP (blue and red bars, respectively; N = 10). Plots show whole brain SNR **(A)** and CNR across b-values 1000, 2000 and 3000 **(B)**, as well as three-crossing fiber ratio **(C)** and dispersion uncertainties (in degree) of 1st, 2nd and 3rd fiber orientations in the white matter voxels **(D)**. Overall, the quality measures were comparable across the studies.

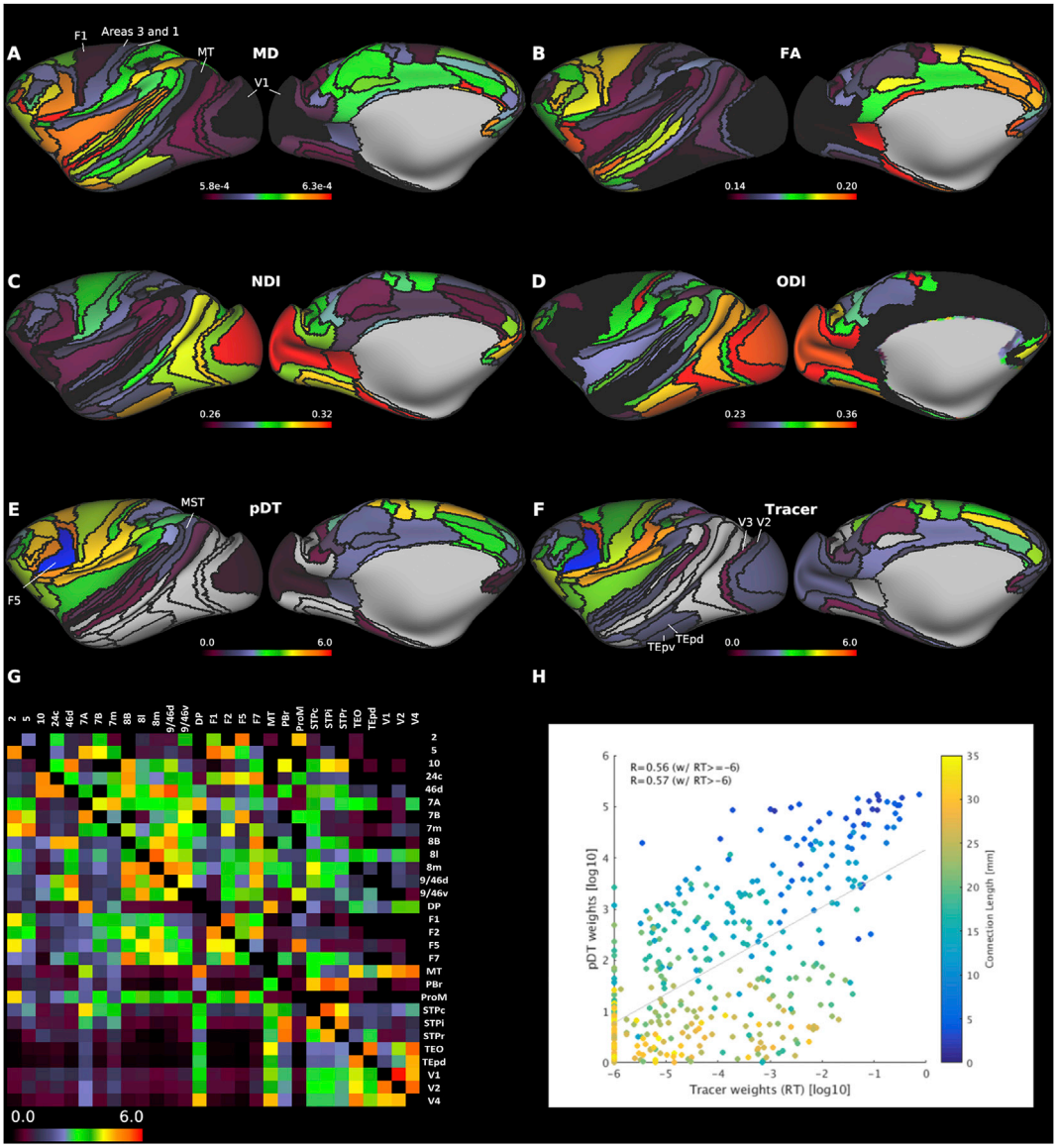

Fig. 9. Representative diffusion magnetic resonance imaging (dMRI) applications. Parcellated cortical surface distributions of mean diffusivity (MD) **(A)** and fractional anisotropy (FA) **(B)** calculated in diffusion tensor model, and neurite density index (NDI) and **(C)** orientation dispersion index (ODI) **(D)** calculated in NODDI (see main text; N = 6). **(E)** Parcellated diffusion tractography (pDT, N = 1, ID = A18031601) seed from left premotor area, F5 (blue color). **(F)** Retrograde tracer (RT) connectivity from F5. Color bars in pDT and RT are scaled in log10 units. **(G)** Comparison of the bidirectional 29x 29 connectivity matrices between pDT (lower diagonal, averaged across) and tracer (upper diagonal) (see Fig. S1 in Markov et al., 2014 or at www.core-nets.org for cortical location of 29 areal parcellations). **(H)** RT vs pDT connectivity weights (number of connections = 406). Color bar indicate the white matter connection length between the parcels. In F and G, the tracer connectivity weights (FLNe in $\log_{10}$) are shown in the actual values plus 6 for visualization purpose. Data at https://balsa.wustl.edu/zppXg.

4.1. Coil design

Our multichannel receive coil, fabricated to closely fit a large macaque head (Fig. 1A) will allow routine imaging of macaque monkeys of different species with a range of lateral muscles and head sizes. The close proximity of the coil to the head allows high SNR in the brain with further SNR gains in the cortex produced by the small size of the elements (Fig. 1) (Janssens et al., 2013; Wiggins et al., 2006). This design allowed acquisition of both T1w and T2w structural whole-brain image acquisition with a 0.5 mm isotropic resolution in 22 min (Fig. 3a, b). In conjunction with homogeneous RF transmission (Fig. 3C and D), these two features enabled automatic and robust subcortical segmentations and reconstructions of pial and white matter surfaces (Supplementary Fig. S5).

Twenty-four receive elements were arranged so as to optimize efficiency of spatial encoding capability in the axial slice direction (Fig. 1B, D). This geometrical arrangement yields a relatively small noise correlation coefficient (0.084), which is smaller than in previous macaque multi-channel coil designs such as 0.12 in a 24-channel (Gilbert et al., 2016) and 0.22 in a 22-channel (Janssens et al., 2013). Our coil design together with slice and in-plane accelerated imaging allowed up to five-fold and two-by-two (MB-by-GRAPPA) accelerations for fMRI and dMRI, respectively. Moreover, this substantially improved the imaging data quality through increased efficiency in accumulation of data volumes (rfMRI: over 8000 vol; and dMRI: 500 diffusion directions, all acquired in a single session in a period of 140 min). Taken together, our 24-channel coil highlights the benefit of accelerated imaging achieved through the geometrical arrangement and low noise correlation of the coil elements.

The close proximity of the multichannel coil to the animals' head may, however, hamper accommodation of the head-post, chambers, or other recording devices. Nonetheless, work is in progress in our

laboratory to alter the coil design to accommodate head-post, and potentially other devices, enabling awake-state fMRI scans. Alternatively, recent development in non-rigid materials for coil elements (Corea et al., 2016) is a promising avenue which could enable accommodation of additional recording devices.

4.2. Resting-state fMRI

To accurately map BOLD signals onto the cortical sheet, the image resolution (1.25 mm isotropic) was matched with 5th percentile of cortical thickness (Fig. 4N, O, P) to reduce the partial volume effects from white matter and CSF signals (Glasser et al., 2013), following the HCP data acquisition strategy at 3T (resolution 2 mm, the 5th percentile of human cortical thickness). The reduction from an isotropic volume of 2 mm–1.25 mm, however, incurs a 4-fold SNR penalty. Nonetheless, tSNR of fMRI in macaque (Fig. 3G and H) is superior to that in the HCP acquired with comparable imaging parameters (Supplementary Fig. S4; Table S1). This tSNR gain may be primarily attributed to the close proximity to the animal and small diameter of the receive coil elements, with an additional gain from relatively small bandwidth. This illustrates the power of parallel imaging to overcome a physical size difference of a factor of twelve (macaque and human brain volumes are approximately 100 cm^3 and 1200 cm^3, respectively).

While informative, tSNR is not an explicit measure of fMRI sensitivity to blood flow changes induced by neural activity. It is well known that variation of fMRI signal is a mixture of nuisance (e.g. motion and respiration) and neural BOLD components. To obtain insight into the content of our fMRI signals, we categorized different signal sources and found that neural BOLD signal explains approximately 4.1% of the total fMRI variance (in data grand mean scaled to 10,000; corresponding to 773 ± 438 in absolute variance) in anesthetized macaque resting-state (Fig. 6). In HCP fMRI data (awake-state), neural BOLD signal explains approximately 7.7% of total variance (corresponding to 4158 ± 1594 in absolute variance (Glasser et al., 2018; Marcus et al., 2013)). Because the image acquisition protocols and image qualities are similar across studies (Supplementary Fig. S4), we speculate that the lower BOLD neural signal in our macaque data may be due to, 1) attenuated thalamo-cortical and cortico-cortical synchronization in the anesthetized state, and/or 2) a ceiling effect of signals due to relatively high blood flow, oxygen extraction rate, and saturation in the anesthetized macaque brain (Kudomi et al., 2005). The latter issue may be overcome with widely used contrast agents (i.e. MION) and cerebral blood volume weighted fMRI (Mandeville et al., 1998) to boost CNR. Nonetheless, the relatively small contribution of neural BOLD signal to the total variance highlights the critical importance of post-processing to clean up nuisance signals to obtain functional connectivity estimates that are neurobiologically meaningful. ICA-based FIX denoising has been established to be very successful at removing non-random time-varying spatially specific artefacts (e.g. movement, vascular and cerebrospinal fluid pulsation or scanning artefacts) in the human resting-state fMRI (Griffanti et al., 2017, 2014; Salimi-Khorshidi et al., 2014; Smith et al., 2013). Here, we demonstrated that FIX is also very successful at reducing such artefacts (6.0% of total variance, Fig. 6) with over 98% classification accuracy (threshold at 20, Table 2) in the macaque resting-state fMRI. The relative global mean variance and its reduction in macaque (1.5% before cleanup and 1.0% after cleanup) is smaller in comparison to the HCP (3.2% before cleanup and 2.2% after cleanup) (Glasser et al., 2018). This smaller global signal variance in anesthetized macaques can be attributed to more stable global blood flow because respiration and pCO_2 were regulated by mechanical ventilation (Birn et al., 2006). The majority of the signal variance, however, is unstructured noise (>60%), particularly in subcortical regions that are distant from the coil elements (Supplementary Fig. S7), which can be effectively reduced by averaging within parcels and/or applying Wishart filtering (Fig. 8B) (Glasser et al., 2016b).

The advantages of our experimental approach was further demonstrated by the capability to identify an average (across sessions/animals) of 22 ± 9 signal (neural) components at 3T (Fig. 7, for exemplar signal components see Fig. 7 or in BALSA at https://balsa.wustl.edu/3ggwG). A previous report using group-ICA from six anesthetized macaques at 7T identified 11 RSNs (Hutchison et al., 2011). Our preliminary results replicate several of these RSNs. Moreover, in comparison to publicly available macaque datasets meeting the minimum criteria for the HCP-NHP pipeline (high-resolution structural images and B_0 field-map) in PRIME-DE (Milham et al., 2018), our data was superior in functional connectivity metrics, such as number of neural components, BOLD variance ratio, CNR, and it shows considerable promise for exploring seed-based functional connectivity (Supplementary Table S4 and Supplementary Fig. S12, Supplementary Text S1). Taken together, from the data quality perspective, the 24-channel coil yields macaque rfMRI data that can be accurately mapped onto cortical sheet and is comparable in quality with the HCP rfMRI data. However from the physiology perspective, we must be cautious when making inferences because of the potential effects of anesthesia on both neural activity and neurovascular coupling. We will explore this topic in future work on a specialized coil for awake monkey imaging as described above.

While scaling the fMRI resolution with respect to the cortical thickness is a minimum requirement to accurately localize BOLD signal within the cortical sheet, another important factor is the size of functional imaging voxels relative to the area of the cortical surface for identifying sharp gradient ridges in FC (Glasser et al., 2016a). We found that macaque cortical grey matter surface area is ≈ 10,100 mm^2 per hemisphere, which is close to previous estimates of 11,900 mm^2 (Chaplin et al., 2013) and 9,600 mm^2 (Donahue et al., 2018). Given that each cortical hemisphere is estimated to contain 130-140 cortical areas (Van Essen et al., 2012), an average parcel corresponds to an approximate area of 70 mm^2 or 70 greyordinates (in our standard 10k greyordinate per hemisphere space for the macaque with 1.25 mm average spacing between greyordinates). However, macaque cortical areas range widely in size, and many are between 5 and 20 mm^2 (Van Essen et al., 2012) and thus may be represented by only ~5–20 greyordinates. In comparison, each human cortical hemisphere has an approximate area of 88,200 mm^2, about 9-fold greater than in the macaque. Since it has 180 cortical areas (Glasser et al., 2016a), an average human cortical parcel corresponds to an area of 490 mm^2 or ≈160 greyordinates (in the HCP standard 32k greyordinates per hemisphere space for humans), albeit many fewer for the smallest human areas. This suggests that consistently identifying distinct gradient ridges along areal boundaries may be much more challenging for the macaque than it was for humans, owing to the lower number of greyordinates for small areas. Viewed from another perspective, since macaque cortex contains 0.85 billion neurons per hemisphere (Herculano-Houzel et al., 2007), a single greyordinate (in 10k space) samples about 85,000 neurons on average. In comparison, since human cortex contain 8.2 billion neurons per hemisphere (Azevedo et al., 2009), so a single HCP greyordinate (in 32k space) samples an average of 270,000 neurons, about three-fold greater than in the macaque. Taken together, while the expected number of greyordinates per cortical area is larger in the human (due to 9-fold larger cortical area of the human brain), our HCP-style approach for the macaque samples fewer neurons per greyordinate (due to the 4-fold smaller voxel volume).

4.3. Diffusion MRI

Spatial resolution is among the most important factors for resolving crossing fiber architecture (Donahue et al., 2016) and microstructural properties such as cortical radial anisotropy (Fan et al., 2017; Sotiropoulos et al., 2016). The ratio between the voxel size and macaque white matter volume for the presented dMRI protocol (0.73 mm^3/23.000 $mm^3 \approx 3 \times 10^{-5}$) approximately matches 2.5 mm isotropic resolution in the human white matter (16 mm^3/500.000 $mm^3 \approx 3 \times 10^{-5}$) but is an order of magnitude larger than in the HCP (1.95 mm^3/500.000 $mm^3 \approx 4 \times 10^{-6}$), although a more precise comparison would require investigations on features such as radii of curvature, tract

and blade thickness. Smaller voxel size could aid in distinguishing challenging fiber pathways, however, under our experimental conditions further reduction was impractical due to gradient power and SNR limitations.

To mitigate this limitation, our strategy was to acquire data with exceptionally high angular resolution (500 directions) capitalizing on two-by-two acceleration (out-of-plane MB and in-plane GRAPPA) enabled by the multichannel array coil. The effect of this strategy was shown in the comparable sensitivity to 3rd crossing fibers between species (Fig. 8), despite the resolution limitation in macaque. A recent ex vivo macaque study used high-quality, high-field magnetic field (4.7T), long data acquisition (≈27 h) postmortem and gadolinium enhanced diffusion scans to demonstrate a modestly informative correspondence between probabilistic tractography and quantitative retrograde tracer ($R = 0.59–0.61$) (Donahue et al., 2016). Here, we replicated aspects of that analysis (Fig. 9E–H), thus, augmenting the findings of Donahue and colleagues to in vivo applications that are obtained within practical time limitations (≈30 min). Taken together, these results suggest that the 'HCP'-style dMRI data acquisition protocols are well positioned to produce in vivo quantitative tractography measures that are neuroanatomically meaningful.

The high spatial resolution with respect to cortical thickness enabled us to carry out cortical surface mapping of neurite properties and to provide preliminary evidence for nonuniformity in the composition and distribution of neurites in macaque cerebral cortex (Fig. 9C and D). Neurite properties are considered important because the density of neurites constitute basic building units (axons and dendrites) of neuronal networks, while ODI provides an indicator of the heterogeneity of neurite fiber orientations, a ratio between tangential and radial fibers (Fukutomi et al., 2018). We found that NDI was highest in V1 and higher than average in other visual representation areas (V2, V3, V4, and MT), somatosensory (1, 2, 3 and A1), motor (F1) and granular prefrontal (Fig. 9C), cortical distributions resembled those of myelin contrast (Fig. 4L). ODI was high in early somatosensory, auditory and visual cortices (Fig. 9D). Together, these results are in good agreement with the HCP data (Fukutomi et al., 2018, 2019).

4.4. Towards improved macaque connectomes and cross-species connectome comparisons

The construction of a high-quality connectome requires anatomically accurate definitions of parcels that represent a biologically meaningful partition of brain areas based on their function, architecture, connectivity, and topography (Felleman and Van Essen, 1991; Glasser et al., 2016a; Van Essen and Glasser, 2018). Comparison between transitions in multimodal neuroimaging contrasts, such as MT myelination (Fig. 4C) and functional connectivity (Fig. 8A, E), are particularly suggestive of brain area boundaries (Glasser et al., 2016a). Therefore, the approach to data collection and analysis presented here provides macaque data that may aid in multi-modal parcellation of the macaque and generation of structural and functional connectomes (Glasser et al., 2016b), though a robust delineation of cortical areas into functionally distinct areas will assuredly require analysis of a more extensive neuroimaging dataset and will likely require additional types of data such as from high resolution postmortem histology.

These HCP-style macaque data also provide an attractive substrate for multi-modal registration across species—in particular, macaques and humans. Just as myelin maps and resting state networks are used to register across human subjects (Robinson et al., 2018, 2014), they could be used to register the cerebral cortex between group averages of humans and macaques. This would allow direct comparisons between human and macaque structural and functional connectivity (Mars et al., 2018b). That said, we expect that the gains for cross-individual registration with areal features in the macaque will be less than those in humans simply because folding patterns and the relationships between folds and areas are less variable in macaques than they are in humans (Van Essen et al., 2019). Additionally, this approach to macaque imaging acquisition and analysis can be used to generate structural and functional connectomes in the macaque for comparison with invasively measured tracer datasets (Donahue et al., 2016; Glasser et al., 2016b). Such validation analyses will help to establish optimal methods for estimating structural and functional connectomes in humans (Jbabdi et al., 2013), where a direct comparison with a gold standard is not available. Future work will also explore cross-species comparisons (Eichert et al., 2019; Norman--Haignere et al., 2019; Premereur et al., 2018; Xu et al., 2019) between alert macaques and marmosets imaged using specialized hardware and an HCP-style approach. These acquisition and analysis methods can also be applied to study disease models in primate species where controlled and invasive methods can be used to investigate causality and plasticity of structural and functional connectomes and their importance in shaping primate behavior.

5. Conclusions

A 24-channel phased-array coil for 3T was constructed and optimized for in vivo parallel imaging of macaque monkey brain. The coil provided high SNR whole-brain coverage and allowed parallel imaging with high-speed acquisition by a five-fold and four-fold increase in functional and diffusion MRI, respectively. The data acquisition strategy in combination with the HCP-NHP minimal preprocessing pipelines enabled robust mapping of structural and functional properties onto the cortical surface. The presented protocols can be acquired within a single imaging session and represent a compelling advance in characterizing multi-modal cortical organization and structural and functional connectomes in the macaque. Overall, this study demonstrates that MRI studies in animals can benefit from adapting the methodologies introduced by the HCP.

Notes

Data of figures and supplementary figures are available at https://balsa.wustl.edu/study/show/LPDP.

Raw data associated with this publication are available at PRIME-DE (http://fcon_1000.projects.nitrc.org/indi/indiPRIME.html). Supplementary Information is available in the online version of the paper. These datasets require Connectome Workbench v1.4.2 for visualization.

CRediT authorship contribution statement

Joonas A. Autio: Investigation, Formal analysis, Writing - original draft. **Matthew F. Glasser:** Conceptualization, Formal analysis, Software, Writing - original draft, Writing - review & editing. **Takayuki Ose:** Investigation. **Chad J. Donahue:** Software, Writing - review & editing. **Matteo Bastiani:** Software, Writing - review & editing. **Masahiro Ohno:** Investigation. **Yoshihiko Kawabata:** Methodology. **Yuta Urushibata:** Investigation, Formal analysis. **Katsutoshi Murata:** Investigation, Formal analysis. **Kantaro Nishigori:** Investigation. **Masataka Yamaguchi:** Investigation. **Yuki Hori:** Formal analysis. **Atsushi Yoshida:** Investigation. **Yasuhiro Go:** Investigation. **Timothy S. Coalson:** Software, Writing - review & editing. **Saad Jbabdi:** Software, Writing - review & editing. **Stamatios N. Sotiropoulos:** Software, Writing - review & editing. **Henry Kennedy:** Data curation, Writing - review & editing, Funding acquisition. **Stephen Smith:** Software, Writing - review & editing. **David C. Van Essen:** Writing - review & editing, Supervision, Funding acquisition. **Takuya Hayashi:** Conceptualization, Investigation, Data curation, Formal analysis, Funding acquisition, Software, Resources, Project administration, Writing - original draft, Writing - review & editing.

Acknowledgements

We thank technical help and comments from Yujie Hou, Kenneth Knoblauch, Stephen Frey, Nobuyoshi Tanki, Chiho Takeda, Akihiro

Kawasaki, Reiko Kobayashi, Kenji Mitsui and Hanako Hirose for their technical help. This research is partially supported by the program for Brain/MINDS and Brain/MINDS-beyond from Japan Agency for Medical Research and development, AMED (JP18dm0207001, JP19dm0307006), by RIKEN Compass to Healthy Life Research Complex Program from Japan Science and Technology Agency, JST, by MEXT KAKENHI Grant (16H03300, 16H03306, 16H01626, 15K12779 (T.H.) and JP26640065, JP16H06531 (Y.G.), NIH F30 MH097312 (M.F.G.), T32 EB014855 (C.J.D.), and RO1 MH-060974 (D.C.V.E.), by the National Institutes of Natural Sciences (NINS) program for cross-disciplinary study (2013–2015) (Y.G.) and by Wellcome Trust (SMS, JS) and by LABEX CORTEX (ANR-11-LABX-0042) of Université de Lyon (ANR-11-IDEX-0007) operated by the French National Research Agency (ANR) (H. K.), ANR-11-BSV4-501, CORE-NETS (H.K.), ANR-14-CE13-0033, ARCHI-CORE (H.K.), ANR-15-CE32-0016, CORNET (H.K.), Chinese Academy of Sciences President's International Felloship Initiative. Grant No. 2018VBA0011 (H.K.). The author Yoshihiko Kawabata holds financial conflict of interest because the coil is produced by his company (Takashima Seisakusho Co. Ltd., Tokyo, Japan) and distributed through his collaboration company (Rogue Research, Montreal, Canada). The other authors have no conflicts of interest to declare.

Appendix A. Supplementary data

Supplementary data to this article can be found online at https://doi.org/10.1016/j.neuroimage.2020.116800.

References

Andersson, J.L.R., Skare, S., Ashburner, J., 2003. How to correct susceptibility distortions in spin-echo echo-planar images: application to diffusion tensor imaging. Neuroimage 20, 870–888. https://doi.org/10.1016/S1053-8119(03)00336-7.

Andersson, J.L.R., Sotiropoulos, S.N., 2016. An integrated approach to correction for off-resonance effects and subject movement in diffusion MR imaging. Neuroimage 125, 1063–1078.

Andersson, J.L.R., Sotiropoulos, S.N., 2015. Non-parametric representation and prediction of single- and multi-shell diffusion-weighted MRI data using Gaussian processes. Neuroimage 122, 166–176. https://doi.org/10.1016/j.neuroimage.2015.07.067.

Azevedo, F.A.C., Carvalho, L.R.B., Grinberg, L.T., Farfel, J.M., Ferretti, R.E.L., Leite, R.E.P., Filho, W.J., Lent, R., Herculano-Houzel, S., 2009. Equal numbers of neuronal and nonneuronal cells make the human brain an isometrically scaled-up primate brain. J. Comp. Neurol. 513, 532–541. https://doi.org/10.1002/cne.21974.

Bastiani, M., Cottaar, M., Fitzgibbon, S.P., Suri, S., Alfaro-Almagro, F., Sotiropoulos, S.N., Jbabdi, S., Andersson, J.L.R., 2019. Automated quality control for within and between studies diffusion MRI data using a non-parametric framework for movement and distortion correction. Neuroimage 184, 801–812. https://doi.org/10.1016/j.neuroimage.2018.09.073.

Behrens, T.E.J., Berg, H.J., Jbabdi, S., Rushworth, M.F.S., Woolrich, M.W., 2007. Probabilistic diffusion tractography with multiple fibre orientations: what can we gain? Neuroimage 34, 144–155. https://doi.org/10.1016/j.neuroimage.2006.09.018.

Birn, R.M., Diamond, J.B., Smith, M.A., Bandettini, P.A., 2006. Separating respiratory-variation-related fluctuations from neuronal-activity-related fluctuations in fMRI. Neuroimage 31, 1536–1548. https://doi.org/10.1016/j.neuroimage.2006.02.048.

Brodmann, K., 1905. Beitrage zur histologischen localisation der grosshirnrinde. Dritte Mitteilung. Die Rinden-felder der niederen Affen. J. Psychol. Neurol. 177–226.

Cauley, S.F., Polimeni, J.R., Bhat, H., Wald, L.L., Setsompop, K., 2014. Interslice leakage artifact reduction technique for simultaneous multislice acquisitions. Magn. Reson. Med. 72, 93–102. https://doi.org/10.1002/mrm.24898.

Chaplin, T.A., Yu, H.-H., Soares, J.G.M., Gattass, R., Rosa, M.G.P., 2013. A conserved pattern of differential expansion of cortical areas in simian primates. J. Neurosci. 33, 15120–15125. https://doi.org/10.1523/JNEUROSCI.2909-13.2013.

Coalson, T.S., Van Essen, D.C., Glasser, M., 2018. Lost in space: the impact of traditional neuroimaging methods on the spatial localization of cortical areas. https://doi.org/10.1101/255620.

Corea, J.R., Flynn, A.M., Lechêne, B., Scott, G., Reed, G.D., Shin, P.J., Lustig, M., Arias, A.C., 2016. Screen-printed flexible MRI receive coils. Nat. Commun. 7, 1–7. https://doi.org/10.1038/ncomms10839.

Donahue, C.J., Glasser, M.F., Preuss, T.M., Rilling, J.K., Essen, D.C.V., 2018. Quantitative assessment of prefrontal cortex in humans relative to nonhuman primates. Proc. Natl. Acad. Sci. Unit. States Am. https://doi.org/10.1073/pnas.1721653115, 201721653.

Donahue, C.J., Sotiropoulos, S.N., Jbabdi, S., Hernandez-Fernandez, M., Behrens, T.E., Dyrby, T.B., Coalson, T., Kennedy, H., Knoblauch, K., Essen, D.C.V., Glasser, M.F., 2016. Using diffusion tractography to predict cortical connection strength and distance: a quantitative comparison with tracers in the monkey. J. Neurosci. 36, 6758–6770. https://doi.org/10.1523/JNEUROSCI.0493-16.2016.

Eichert, N., Robinson, E.C., Bryant, K.L., Jbabdi, S., Jenkinson, M., Li, L., Krug, K., Watkins, K.E., Mars, R.B., 2019. Cross-species cortical alignment identifies different types of neuroanatomical reorganization in higher primates. bioRxiv 645234. https://doi.org/10.1101/645234.

Fan, Q., Nummenmaa, A., Polimeni, J.R., Witzel, T., Huang, S.Y., Wedeen, V.J., Rosen, B.R., Wald, L.L., 2017. HIgh b-value and high Resolution Integrated Diffusion (HIBRID) imaging. Neuroimage 150, 162–176. https://doi.org/10.1016/j.neuroimage.2017.02.002.

Felleman, D.J., Van Essen, D., 1991. Distributed hierarchical processing in the primate cerebral cortex. Cereb. Cortex N. Y. N 1, 1–47. https://doi.org/10.1093/cercor/1.1.1, 1991.

Fischl, B., 2012. FreeSurfer. NeuroImage, 20 YEARS OF fMRI20 YEARS. OF fMRI 62, 774–781. https://doi.org/10.1016/j.neuroimage.2012.01.021.

Fukutomi, H., Glasser, M.F., Murata, K., Akasaka, T., Fujimoto, K., Yamamoto, T., Autio, J.A., Okada, T., Togashi, K., Zhang, H., Van Essen, D.C., Hayashi, T., 2019. Diffusion Tensor Model links to Neurite Orientation Dispersion and Density Imaging at high b-value in. Cerebral Cortical Gray Matter. Sci Rep 9, 12246. https://doi.org/10.1038/s41598-019-48671-7.

Fukutomi, H., Glasser, M.F., Zhang, H., Autio, J.A., Coalson, T.S., Okada, T., Togashi, K., Van Essen, D.C., Hayashi, T., 2018. Neurite imaging reveals microstructural variations in human cerebral cortical gray matter. Neuroimage. https://doi.org/10.1016/j.neuroimage.2018.02.017.

Mareyam, A., Gao, Y., Sun, Y., Witzel, T., Arango, N., Kuang, I., White, J., Roe, A.W., Wald, L., Stockmann, J., Zhang, X., 2020. A 16-channel AC/DC array coil for anesthetized monkey whole-brain imaging at 7T. Neuroimage 207, 116396. https://doi.org/10.1016/j.neuroimage.2019.116396.

Gilbert, K.M., Gati, J.S., Barker, K., Everling, S., Menon, R.S., 2016. Optimized parallel transmit and receive radiofrequency coil for ultrahigh-field MRI of monkeys. Neuroimage 125, 153–161. https://doi.org/10.1016/j.neuroimage.2015.10.048.

Glasser, M.F., Coalson, T.S., Bijsterbosch, J.D., Harrison, S.J., Harms, M.P., Anticevic, A., Van Essen, D.C., Smith, S.M., 2018. Using temporal ICA to selectively remove global noise while preserving global signal in functional MRI data. Neuroimage 181, 692–717. https://doi.org/10.1016/j.neuroimage.2018.04.076.

Glasser, M.F., Coalson, T.S., Robinson, E.C., Hacker, C.D., Harwell, J., Yacoub, E., Ugurbil, K., Andersson, J., Beckmann, C.F., Jenkinson, M., Smith, S.M., Van Essen, D.C., 2016a. A multi-modal parcellation of human cerebral cortex. Nature 536, 171–178. https://doi.org/10.1038/nature18933.

Glasser, M.F., Goyal, M.S., Preuss, T.M., Raichle, M.E., Van Essen, D.C., 2014. Trends and properties of human cerebral cortex: correlations with cortical myelin content. NeuroImage, In-vivo Brodmann Mapping of the Human Brain. Neuroimage 93 (2), 165–175. https://doi.org/10.1016/j.neuroimage.2013.03.060.

Glasser, M.F., Smith, S.M., Marcus, D.S., Andersson, J.L.R., Auerbach, E.J., Behrens, T.E.J., Coalson, T.S., Harms, M.P., Jenkinson, M., Moeller, S., Robinson, E.C., Sotiropoulos, S.N., Xu, J., Yacoub, E., Ugurbil, K., Essen, D.C.V., 2016b. The Human Connectome Project's neuroimaging approach. Nat. Neurosci. 19, 1175–1187. https://doi.org/10.1038/nn.4361.

Glasser, M.F., Sotiropoulos, S.N., Wilson, J.A., Coalson, T.S., Fischl, B., Andersson, J.L., Xu, J., Jbabdi, S., Webster, M., Polimeni, J.R., Van Essen, D.C., Jenkinson, M., 2013. The minimal preprocessing pipelines for the Human Connectome Project. Neuroimage 80, 105–124. https://doi.org/10.1016/j.neuroimage.2013.04.127.

Glasser, M.F., Van Essen, D.C., 2011. Mapping human cortical areas in vivo based on myelin content as revealed by T1- and T2-weighted MRI. J. Neurosci. 31, 11597–11616. https://doi.org/10.1523/JNEUROSCI.2180-11.2011.

Goense, J.B.M., Logothetis, N.K., 2008. Neurophysiology of the BOLD fMRI signal in awake monkeys. Curr. Biol. 18, 631–640. https://doi.org/10.1016/j.cub.2008.03.054.

Gomori, J.M., Holland, G.A., Grossman, R.I., Gefter, W.B., Lenkinski, R.E., 1988. Fat suppression by section-select gradient reversal on spin-echo MR imaging. Work progress. Radiol 168, 493–495. https://doi.org/10.1148/radiology.168.2.3393670.

Gonzalez-Castillo, J., Duthie, K.N., Saad, Z.S., Chu, C., Bandettini, P.A., Luh, W.-M., 2013. Effects of image contrast on functional MRI image registration. Neuroimage 67, 163–174. https://doi.org/10.1016/j.neuroimage.2012.10.076.

Greve, D.N., Fischl, B., 2009. Accurate and robust brain image alignment using boundary-based registration. Neuroimage 48, 63–72. https://doi.org/10.1016/j.neuroimage.2009.06.060.

Griffanti, L., Douaud, G., Bijsterbosch, J., Evangelisti, S., Alfaro-Almagro, F., Glasser, M.F., Duff, E.P., Fitzgibbon, S., Westphal, R., Carone, D., Beckmann, C.F., Smith, S.M., 2017. Hand Classification of fMRI ICA Noise Components. NeuroImage, Cleaning up the fMRI Time Series: Mitigating Noise with Advanced Acquisition and Correction Strategies, 154, pp. 188–205. https://doi.org/10.1016/j.neuroimage.2016.12.036.

Griffanti, L., Salimi-Khorshidi, G., Beckmann, C.F., Auerbach, E.J., Douaud, G., Sexton, C.E., Zsoldos, E., Ebmeier, K.P., Filippini, N., Mackay, C.E., Moeller, S., Xu, J., Yacoub, E., Baselli, G., Ugurbil, K., Miller, K.L., Smith, S.M., 2014. ICA-based artefact removal and accelerated fMRI acquisition for improved resting state network imaging. Neuroimage 95, 232–247. https://doi.org/10.1016/j.neuroimage.2014.03.034.

Griswold, M.A., Jakob, P.M., Heidemann, R.M., Nittka, M., Jellus, V., Wang, J., Kiefer, B., Haase, A., 2002. Generalized autocalibrating partially parallel acquisitions (GRAPPA). Magn. Reson. Med. 47, 1202–1210. https://doi.org/10.1002/mrm.10171.

Guldenmund, P., Vanhaudenhuyse, A., Sanders, R.D., Sleigh, J., Bruno, M.A., Demertzi, A., Bahri, M.A., Jaquet, O., Sanfilippo, J., Baquero, K., Boly, M., Brichant, J.F., Laureys, S., Bonhomme, V., 2017. Brain functional connectivity differentiates dexmedetomidine from propofol and natural sleep. Br. J. Anaesth. 119, 674–684. https://doi.org/10.1093/bja/aex257.

Helms, G., Garea-Rodriguez, E., Schlumbohm, C., König, J., Dechent, P., Fuchs, E., Wilke, M., 2013. Structural and quantitative neuroimaging of the common marmoset monkey using a clinical MRI system. J. Neurosci. Methods 215, 121–131. https://doi.org/10.1016/j.jneumeth.2013.02.011.

Herculano-Houzel, S., Collins, C.E., Wong, P., Kaas, J.H., 2007. Cellular scaling rules for primate brains. Proc. Natl. Acad. Sci. Unit. States Am. 104, 3562–3567. https://doi.org/10.1073/pnas.0611396104.

Hernández, M., Guerrero, G.D., Cecilia, J.M., García, J.M., Inuggi, A., Jbabdi, S., Behrens, T.E.J., Sotiropoulos, S.N., 2013. Accelerating fibre orientation estimation from diffusion weighted magnetic resonance imaging using GPUs. PloS One 8, e61892. https://doi.org/10.1371/journal.pone.0061892.

Hernandez-Fernandez, M., Reguly, I., Jbabdi, S., Giles, M., Smith, S., Sotiropoulos, S.N., 2018. Using GPUs to accelerate computational diffusion MRI: from microstructure estimation to tractography and connectomes. Neuroimage 188, 598–615. https://doi.org/10.1016/j.neuroimage.2018.12.015.

Hutchison, R.M., Leung, L.S., Mirsattari, S.M., Gati, J.S., Menon, R.S., Everling, S., 2011. Resting-state networks in the macaque at 7 T. Neuroimage 56, 1546–1555. https://doi.org/10.1016/j.neuroimage.2011.02.063.

Janssens, T., Keil, B., Serano, P., Mareyam, A., McNab, J.A., Wald, L.L., Vanduffel, W., 2013. A 22-channel receive array with Helmholtz transmit coil for anesthetized macaque MRI at 3 T. NMR Biomed. 26, 1431–1440. https://doi.org/10.1002/nbm.2970.

Jbabdi, S., Lehman, J.F., Haber, S.N., Behrens, T.E., 2013. Human and monkey ventral prefrontal fibers use the same organizational principles to reach their targets: tracing versus tractography. J. Neurosci. Off. J. Soc. Neurosci. 33, 3190–3201. https://doi.org/10.1523/JNEUROSCI.2457-12.2013.

Jbabdi, S., Sotiropoulos, S.N., Savio, A.M., Graña, M., Behrens, T.E.J., 2012. Model-based analysis of multishell diffusion MR data for tractography: how to get over fitting problems. Magn. Reson. Med. 68, 1846–1855. https://doi.org/10.1002/mrm.24204.

Jenkinson, M., Bannister, P., Brady, M., Smith, S., 2002. Improved optimization for the robust and accurate linear registration and motion correction of brain images. Neuroimage 17, 825–841. https://doi.org/10.1006/nimg.2002.1132.

Khachaturian, M.H., 2010. A 4-channel 3 Tesla phased array receive coil for awake rhesus monkey fMRI and diffusion MRI experiments. J. Biomed. Sci. Eng. 3, 1085–1092. https://doi.org/10.4236/jbise.2010.311141.

Kudomi, N., Hayashi, T., Teramoto, N., Watabe, H., Kawachi, N., Ohta, Y., Kim, K.M., Iida, H., 2005. Rapid quantitative measurement of CMRO2 and CBF by dual administration of 15O-labeled oxygen and water during a single PET scan—a validation study and error analysis in anesthetized monkeys. J. Cerebr. Blood Flow Metabol. 25, 1209–1224. https://doi.org/10.1038/sj.jcbfm.9600118.

Mandeville, J.B., Marota, J.J.A., Kosofsky, B.E., Keltner, J.R., Weissleder, R., Rosen, B.R., Weisskoff, R.M., 1998. Dynamic functional imaging of relative cerebral blood volume during rat forepaw stimulation. Magn. Reson. Med. 39, 615–624. https://doi.org/10.1002/mrm.1910390415.

Marcus, D.S., Harms, M.P., Snyder, A.Z., Jenkinson, M., Wilson, J.A., Glasser, M.F., Barch, D.M., Archie, K.A., Burgess, G.C., Ramaratnam, M., Hodge, M., Horton, W., Herrick, R., Olsen, T., McKay, M., House, M., Hileman, M., Reid, E., Harwell, J., Coalson, T., Schindler, J., Elam, J.S., Curtiss, S.W., Van Essen, D.C., 2013. Human Connectome Project informatics: quality control, database services, and data visualization. Neuroimage 80, 202–219. https://doi.org/10.1016/j.neuroimage.2013.05.077.

Markov, N.T., Ercsey-Ravasz, M.M., Gomes, R., R, A., Lamy, C., Magrou, L., Vezoli, J., Misery, P., Falchier, A., Quilodran, R., Gariel, M.A., Sallet, J., Gamanut, R., Huissoud, C., Clavagnier, S., Giroud, P., Sappey-Marinier, D., Barone, P., Dehay, C., Toroczkai, Z., Knoblauch, K., Essen, V., C, D., Kennedy, H., 2014. A weighted and directed interareal connectivity matrix for macaque cerebral cortex. Cerebr. Cortex 24, 17–36. https://doi.org/10.1093/cercor/bhs270.

Mars, R.B., Passingham, R.E., Jbabdi, S., 2018a. Connectivity fingerprints: from areal descriptions to abstract spaces. Trends Cognit. Sci. 22, 1026–1037. https://doi.org/10.1016/j.tics.2018.08.009.

Mars, R.B., Sotiropoulos, S.N., Passingham, R.E., Sallet, J., Verhagen, L., Khrapitchev, A.A., Sibson, N., Jbabdi, S., 2018b. Whole brain comparative anatomy using connectivity blueprints. eLife 7. https://doi.org/10.7554/eLife.35237.

McKeown, M.J., Makeig, S., Brown, G.G., Jung, T.P., Kindermann, S.S., Bell, A.J., Sejnowski, T.J., 1998. Analysis of fMRI data by blind separation into independent spatial components. Hum. Brain Mapp. 6, 160–188.

Mesulam, M.-M., Mufson, E.J., 1982. Insula of the old world monkey. III: efferent cortical output and comments on function. J. Comp. Neurol. 212, 38–52. https://doi.org/10.1002/cne.902120104.

Milham, M.P., Ai, L., Koo, B., Xu, T., Amiez, C., Balezeau, F., Baxter, M.G., Blezer, E.L.A., Brochier, T., Chen, A., Croxson, P.L., Damatac, C.G., Dehaene, S., Everling, S., Fair, D.A., Fleysher, L., Freiwald, W., Froudist-Walsh, S., Griffiths, T.D., Guedj, C., Hadj-Bouziane, F., Ben Hamed, S., Harel, N., Hiba, B., Jarraya, B., Jung, B., Kastner, S., Klink, P.C., Kwok, S.C., Laland, K.N., Leopold, D.A., Lindenfors, P., Mars, R.B., Menon, R.S., Messinger, A., Meunier, M., Mok, K., Morrison, J.H., Nacef, J., Nagy, J., Rios, M.O., Petkov, C.I., Pinsk, M., Poirier, C., Procyk, E., Rajimehr, R., Reader, S.M., Roelfsema, P.R., Rudko, D.A., Rushworth, M.F.S., Russ, B.E., Sallet, J., Schmid, M.C., Schwiedrzik, C.M., Seidlitz, J., Sein, J., Shmuel, A., Sullivan, E.L., Ungerleider, L., Thiele, A., Todorov, O.S., Tsao, D., Wang, Z., Wilson, C.R.E., Yacoub, E., Ye, F.Q., Zarco, W., Zhou, Y., Margulies, D.S., Schroeder, C.E., 2018. An open resource for non-human primate imaging. Neuron 100, 61–74. https://doi.org/10.1016/j.neuron.2018.08.039 e2.

Moeller, S., Yacoub, E., Olman, C.A., Auerbach, E., Strupp, J., Harel, N., Uğurbil, K., 2010. Multiband multislice GE-EPI at 7 tesla, with 16-fold acceleration using partial parallel imaging with application to high spatial and temporal whole-brain fMRI. Magn. Reson. Med. 63, 1144–1153. https://doi.org/10.1002/mrm.22361.

Mugler, J.P., Bao, S., Mulkern, R.V., Guttmann, C.R.G., Robertson, R.L., Jolesz, F.A., Brookeman, J.R., 2000. Optimized single-slab three-dimensional spin-echo MR imaging of the brain. Radiology 216, 891–899. https://doi.org/10.1148/radiology.216.3.r00au46891.

Mugler, J.P., Brookeman, J.R., 1990. Three-dimensional magnetization-prepared rapid gradient-echo imaging (3D MP RAGE). Magn. Reson. Med. 15, 152–157. https://doi.org/10.1002/mrm.1910150117.

Nei, M., Glazko, G.V., 2002. The wilhelmine E. Key 2001 invitational lecture. Estimation of divergence times for a few mammalian and several primate species. J. Hered. 93, 157–164. https://doi.org/10.1093/jhered/93.3.157.

Norman-Haignere, S.V., Kanwisher, N., McDermott, J.H., Conway, B.R., 2019. Divergence in the functional organization of human and macaque auditory cortex revealed by fMRI responses to harmonic tones. Nat. Neurosci. 22, 1057. https://doi.org/10.1038/s41593-019-0410-7.

Pan, W.-J., Billings, J.C.W., Grooms, J.K., Shakil, S., Keilholz, S.D., 2015. Considerations for resting state functional MRI and functional connectivity studies in rodents. Front. Neurosci. 9, 269. https://doi.org/10.3389/fnins.2015.00269.

Passingham, R., 2009. How good is the macaque monkey model of the human brain? Curr. Opin. Neurobiol. Cognit. Neurosci. 19, 6–11. https://doi.org/10.1016/j.conb.2009.01.002.

Power, J.D., 2016. A simple but useful way to assess fMRI scan qualities. Neuroimage 154, 154–158. https://doi.org/10.1016/j.neuroimage.2016.08.009.

Power, J.D., Mitra, A., Laumann, T.O., Snyder, A.Z., Schlaggar, B.L., Petersen, S.E., 2014. Methods to detect, characterize, and remove motion artifact in resting state fMRI. Neuroimage 84, 320–341. https://doi.org/10.1016/j.neuroimage.2013.08.048.

Premereur, E., Janssen, P., Vanduffel, W., 2018. Functional MRI in macaque monkeys during task switching. J. Neurosci. 38, 10619–10630. https://doi.org/10.1523/JNEUROSCI.1539-18.2018.

Rilling, J.K., Glasser, M.F., Preuss, T.M., Ma, X., Zhao, T., Hu, X., Behrens, T.E.J., 2008. The evolution of the arcuate fasciculus revealed with comparative DTI. Nat. Neurosci. 11, 426–428. https://doi.org/10.1038/nn2072.

Risk, B.B., Kociuba, M.C., Rowe, D.B., 2018. Impacts of simultaneous multislice acquisition on sensitivity and specificity in fMRI. Neuroimage 172, 538–553. https://doi.org/10.1016/j.neuroimage.2018.01.078.

Robinson, E.C., Garcia, K., Glasser, M.F., Chen, Z., Coalson, T.S., Makropoulos, A., Bozek, J., Wright, R., Schuh, A., Webster, M., Hutter, J., Price, A., Cordero Grande, L., Hughes, E., Tusor, N., Bayly, P.V., Van Essen, D.C., Smith, S.M., Edwards, A.D., Hajnal, J., Jenkinson, M., Glocker, B., Rueckert, D., 2018. Multimodal surface matching with higher-order smoothness constraints. Neuroimage 167, 453–465. https://doi.org/10.1016/j.neuroimage.2017.10.037.

Robinson, E.C., Jbabdi, S., Glasser, M.F., Andersson, J., Burgess, G.C., Harms, M.P., Smith, S.M., Van Essen, D.C., Jenkinson, M., 2014. MSM: a new flexible framework for Multimodal Surface Matching. Neuroimage 100, 414–426. https://doi.org/10.1016/j.neuroimage.2014.05.069.

Salimi-Khorshidi, G., Douaud, G., Beckmann, C.F., Glasser, M.F., Griffanti, L., Smith, S.M., 2014. Automatic denoising of functional MRI data: combining independent component analysis and hierarchical fusion of classifiers. Neuroimage 90, 449–468. https://doi.org/10.1016/j.neuroimage.2013.11.046.

Setsompop, K., Cohen-Adad, J., Gagoski, B.A., Raij, T., Yendiki, A., Keil, B., Wedeen, V.J., Wald, L.L., 2012. Improving diffusion MRI using simultaneous multi-slice echo planar imaging. Neuroimage 63, 569–580. https://doi.org/10.1016/j.neuroimage.2012.06.033.

Smith, R.E., Tournier, J.-D., Calamante, F., Connelly, A., 2012. Anatomically-constrained tractography: improved diffusion MRI streamlines tractography through effective use of anatomical information. Neuroimage 62, 1924–1938. https://doi.org/10.1016/j.neuroimage.2012.06.005.

Smith, S.M., Beckmann, C.F., Andersson, J., Auerbach, E.J., Bijsterbosch, J., Douaud, G., Duff, E., Feinberg, D.A., Griffanti, L., Harms, M.P., others, 2013. Resting-state fMRI in the human connectome project. Neuroimage 80, 144–168.

Sotiropoulos, S.N., Hernández-Fernández, M., Vu, A.T., Andersson, J.L., Moeller, S., Yacoub, E., Lenglet, C., Ugurbil, K., Behrens, T.E.J., Jbabdi, S., 2016. Fusion in diffusion MRI for improved fibre orientation estimation: an application to the 3T and 7T data of the Human Connectome Project. Neuroimage 134, 396–409. https://doi.org/10.1016/j.neuroimage.2016.04.014.

Sotiropoulos, S.N., Jbabdi, S., Xu, J., Andersson, J.L., Moeller, S., Auerbach, E.J., Glasser, M.F., Hernandez, M., Sapiro, G., Jenkinson, M., Feinberg, D.A., Yacoub, E., Lenglet, C., Van Essen, D.C., Ugurbil, K., Behrens, T.E.J., 2013. Advances in diffusion MRI acquisition and processing in the human connectome project. Neuroimage 80, 125–143. https://doi.org/10.1016/j.neuroimage.2013.05.057.

Stejskal, E.O., Tanner, J.E., 1965. Spin diffusion measurements: spin echoes in the presence of a time-dependent field gradient. J. Chem. Phys. 42, 288. https://doi.org/10.1063/1.1695690.

Uğurbil, K., Xu, J., Auerbach, E.J., Moeller, S., Vu, A.T., Duarte-Carvajalino, J.M., Lenglet, C., Wu, X., Schmitter, S., Van de Moortele, P.F., Strupp, J., Sapiro, G., De Martino, F., Wang, D., Harel, N., Garwood, M., Chen, L., Feinberg, D.A., Smith, S.M., Miller, K.L., Sotiropoulos, S.N., Jbabdi, S., Andersson, J.L.R., Behrens, T.E.J., Glasser, M.F., Van Essen, D.C., Yacoub, E., 2013. Pushing spatial and temporal resolution for functional and diffusion MRI in the Human Connectome Project. Neuroimage 80, 80–104. https://doi.org/10.1016/j.neuroimage.2013.05.012. Mapping the Connectome.

Van de Moortele, P.-F., Akgun, C., Adriany, G., Moeller, S., Ritter, J., Collins, C.M., Smith, M.B., Vaughan, J.T., Uğurbil, K., 2005. B1 destructive interferences and spatial phase patterns at 7 T with a head transceiver array coil. Magn. Reson. Med. 54, 1503–1518. https://doi.org/10.1002/mrm.20708.

Van Essen, D.C., Dierker, D.L., 2007. Surface-based and probabilistic atlases of primate cerebral cortex. Neuron 56, 209–225. https://doi.org/10.1016/j.neuron.2007.10.015.

Van Essen, D., Donahue, C.J., Coalson, T.S., Kennedy, H., Hayashi, T., Glasser, M.F., 2019. Cerebral Cortical Folding, Parcellation, and Connectivity in Humans, Nonhuman Primates and Mice. Proc Natl Acad Sci U S A 116 (52), 26173–26180. https://doi.org/10.1073/pnas.1902299116.

Van Essen, D.C., Glasser, M.F., 2018. Parcellating cerebral cortex: how invasive animal studies inform noninvasive mapmaking in humans. Neuron 99, 640–663. https://doi.org/10.1016/j.neuron.2018.07.002.

Van Essen, D.C., Glasser, M.F., Dierker, D.L., Harwell, J., 2012. Cortical parcellations of the macaque monkey analyzed on surface-based atlases. Cerebr. Cortex 22, 2227–2240. https://doi.org/10.1093/cercor/bhr290.

Van Essen, D.C., Lewis, J.W., Drury, H.A., Hadjikhani, N., Tootell, R.B.H., Bakircioglu, M., Miller, M.I., 2001. Mapping visual cortex in monkeys and humans using surface-based atlases. Vis. Res. 41, 1359–1378. https://doi.org/10.1016/S0042-6989(01)00045-1.

Van Essen, D.C., Smith, J., Glasser, M.F., Elam, J., Donahue, C.J., Dierker, D.L., Reid, E.K., Coalson, T., Harwell, J., 2017. The brain analysis library of spatial maps and atlases (BALSA) database. NeuroImage, Data Sharing Part II 144, 270–274. https://doi.org/10.1016/j.neuroimage.2016.04.002.

Wang, L., Saalmann, Y.B., Pinsk, M.A., Arcaro, M.J., Kastner, S., 2012. Electrophysiological low-frequency coherence and cross-frequency coupling contribute to BOLD connectivity. Neuron 76, 1010–1020. https://doi.org/10.1016/j.neuron.2012.09.033.

Wiggins, G.c., Triantafyllou, C., Potthast, A., Reykowski, A., Nittka, M., Wald, L.l., 2006. 32-channel 3 Tesla receive-only phased-array head coil with soccer-ball element geometry. Magn. Reson. Med. 56, 216–223. https://doi.org/10.1002/mrm.20925.

Wiggins, G.C., Polimeni, J.R., Potthast, A., Schmitt, M., Alagappan, V., Wald, L.L., 2009. 96-Channel receive-only head coil for 3 Tesla: design optimization and evaluation. Magn. Reson. Med. Off. J. Soc. Magn. Reson. Med. Soc. Magn. Reson. Med. 62, 754–762. https://doi.org/10.1002/mrm.22028.

Xu, T., Nenning, K.-H., Schwartz, E., Hong, S.-J., Vogelstein, J.T., Fair, D.A., Schroeder, C.E., Margulies, D.S., Smallwood, J., Milham, M.P., Langs, G., 2019. Cross-species functional alignment reveals evolutionary hierarchy within the connectome. bioRxiv 692616. https://doi.org/10.1101/692616.

Zhang, H., Schneider, T., Wheeler-Kingshott, C.A., Alexander, D.C., 2012. NODDI: practical in vivo neurite orientation dispersion and density imaging of the human brain. Neuroimage 61, 1000–1016. https://doi.org/10.1016/j.neuroimage.2012.03.072.

Zhang, Y., Brady, M., Smith, S., 2001. Segmentation of brain MR images through a hidden Markov random field model and the expectation-maximization algorithm. IEEE Trans. Med. Imag. 20, 45–57. https://doi.org/10.1109/42.906424.

Zhao, F., Holahan, M.A., Houghton, A.K., Hargreaves, R., Evelhoch, J.L., Winkelmann, C.T., Williams, D.S., 2015. Functional imaging of olfaction by CBV fMRI in monkeys: insight into the role of olfactory bulb in habituation. Neuroimage 106, 364–372. https://doi.org/10.1016/j.neuroimage.2014.12.001.